Gondwana Research 81 (2020) 423–444

Contents lists available at ScienceDirect

Gondwana Research

journal homepage: www.elsevier.com/locate/gr

Fossil seamount in southeast Zagros records intraoceanic arc to back-arc transition: New constraints for the evolution of the Neotethys

G. Bonnet [a,b,*], P. Agard [a], H. Whitechurch [c], M. Fournier [a], S. Angiboust [d], B. Caron [a], J. Omrani [e]

[a] Sorbonne Université, CNRS-INSU, Institut des Sciences de la Terre de Paris, ISTeP UMR 7193, F-75005 Paris, France
[b] Earth Research Institute and Department of Earth Science, University of California, Santa Barbara, CA 93106, USA
[c] Institut de Physique du Globe de Strasbourg, EOST-CNRS-UMR 7516, Université de Strasbourg, 67000 Strasbourg, France
[d] Institut de Physique du Globe de Paris, Sorbonne Paris Cité, Université Paris Diderot, CNRS, F-75005 Paris, France
[e] Geological Survey of Iran, Tehran, Iran

ARTICLE INFO

Article history:
Received 12 February 2019
Received in revised form 15 October 2019
Accepted 16 October 2019
Available online 17 December 2019

Handling Editor: A. Festa

ABSTRACT

The Neotethys ocean is transiently involved in two subduction zones during the Late Cretaceous. While the Northern Neotethys subduction zone (below Eurasia) was active from the early Mesozoic until the Eocene, the intra-oceanic Southern Neotethys subduction zone only developed during the Late Cretaceous. We herein document, through a combination of structural, geochemical and geochronological data, the magmatic evolution of a Late Cretaceous supra-subduction ophiolite fragment of the Neotethys (the Siah Kuh massif, Southern Iran), now sandwiched in the Zagros suture zone. Results show that this ophiolite fragment — a subducted yet exceptionally well-preserved seamount — records an evolution from supra-subduction zone magmatism (including island arc tholeiites, boninites and calc-alkaline transitional magmatism) around 87 Ma, to MORB (from E-MORB to N-MORB) magmatism at 78 Ma, and potentially until 73 Ma. We conclude that this seamount initially formed in an arc context and represents either (i) a non-obducted remnant of the Oman ophiolite that experienced a longer-lived magmatic history (prefered hypothesis) or (ii) a piece from the forearc/frontal arc of the Northern margin of the Neotethys. Regardless of its exact original location, the Siah Kuh seamount was later subducted in the Northern Neotethys subduction zone.

1. Introduction

Alike modern ocean floor, ophiolites exposed throughout the world span a range of geochemical signatures, in part reflecting their diverse original tectonic setting: mid-ocean ridges, ocean islands (hotspots), island arcs (Pearce, 2008). On modern ocean floor, seamounts are defined as "geographically isolated topographic feature[s] on the seafloor taller than 100 m, including ones whose summit regions may temporarily emerge above sea level, but not including features that are located on continental shelves or that are part of other major landmasses" (Staudigel et al., 2010). While the majority of these seamounts are thought to have formed through hotspot-fed magmatism (and have ocean island basalt – OIB – affinities, e.g. Hawaiian islands), many of them also form along ocean ridges (e.g. at the East Pacific Rise, Batiza and Vanko, 1984; with mid-ocean ridge basalt – MORB – affinities) and in volcanic arc contexts (e.g. Izu-Bonin arc system, Hochstaedter et al., 2001; with island arc tholeiite – IAT – to calk-alkaline affinities).

Seamounts are however rarely preserved in the geological record of the ocean floor, i.e. within ophiolitic material. Most of them indeed get subducted (Ranero and von Huene, 2000) with only fragments left over (Cloos, 1993), that may even not be recognized as such (unless having an OIB-like signature; e.g. Hauff et al., 1997; John et al., 2010). A few seamounts however escape subduction and are docked in accretionary wedges (e.g. Nicasio Reservoir Terrane, Schnur and Gilbert, 2012) or are shallowly subducted and underplated, but very few are exhumed almost intact. Notable exceptions are the late Paleozoic Anarak and Kabudan seamounts (Bagheri and Stampfli, 2008; Central Iran) and the Mesozoic Snow Mountain (MacPherson, 1983; Franciscan complex, USA), identified according to their structure and OIB signatures.

In the Mesozoic realm of the Neotethys, the geological record is dominated by supra-subduction zone (SSZ) ophiolites, that may represent either forearc ocean floor, oceanic arc or back-arcs (Moghadam and Stern, 2015 and references therein). This preferential record is consistent with the mechanism leading to the obduction of ophiolite, starting from intra-oceanic subduction initiation (Agard et al., 2007; Boudier et al., 1988), forearc spreading (Casey and Dewey, 1984) and leading to continental subduction below the newly formed ophiolite (Searle et al., 2004). Small ocean basins formed in back-arc settings behind

* Corresponding author at: Earth Research Institute and Department of Earth Science, University of California, Santa Barbara, CA 93106, USA.
E-mail address: gbonnet01@gmail.com (G. Bonnet).

https://doi.org/10.1016/j.gr.2019.10.019
1342-937X/

continental stripes are also partly preserved during collision (e.g. Agard et al., 2011; Rossetti et al., 2010).

These ophiolitic fragments therefore preserve essential information regarding subduction processes and magmatic evolution on the seafloor. However (with the exception of the extensively studied Semail ophiolite in Oman), most large-scale ophiolites or ophiolitic "mélanges" exposed in the Zagros-Makran orogens are strongly dismembered (Burg, 2018; Whitechurch et al., 2013).

This makes the recently discovered Siah Kuh seamount (Bonnet et al., 2019a, 2019b) the ideal target to study the continuous evolution and origin of magmatic activity in an ophiolite, with implications for lithosphere formation, mantle heterogeneities and regional geodynamics.

This contribution therefore addresses three major questions:

(1) In the light of geochemical and geochronological data, what is the origin of the Siah Kuh seamount (i.e., mid-ocean ridge seamount, hotspot/plume related, arc-related)?
(2) Does the Siah Kuh seamount preserve evidence for progressive changes in magmatism and/or in the nature of the (mantle) source?
(3) Does this help constrain the former location of the seamount in the Neotethys realm?

To that end, we herein present detailed petrological and geochemical data, i.e. bulk-rock analyses of major, trace elements and Sr-Nd isotopes, as well as dating and Hf isotope analysis of zircons from representative lithologies.

2. Geological setting

2.1. Ocean-floor and arc preservation in the Iran-Oman Neotethys

The Zagros-Makran orogen formed through the closure of an allegedly large oceanic basin, the Neotethys ocean (probably larger than 1000 km, Agard et al., 2011; Barrier and Vrielynck, 2008). Remnants of this basin are found in Oman (including the thoroughly studied Semail

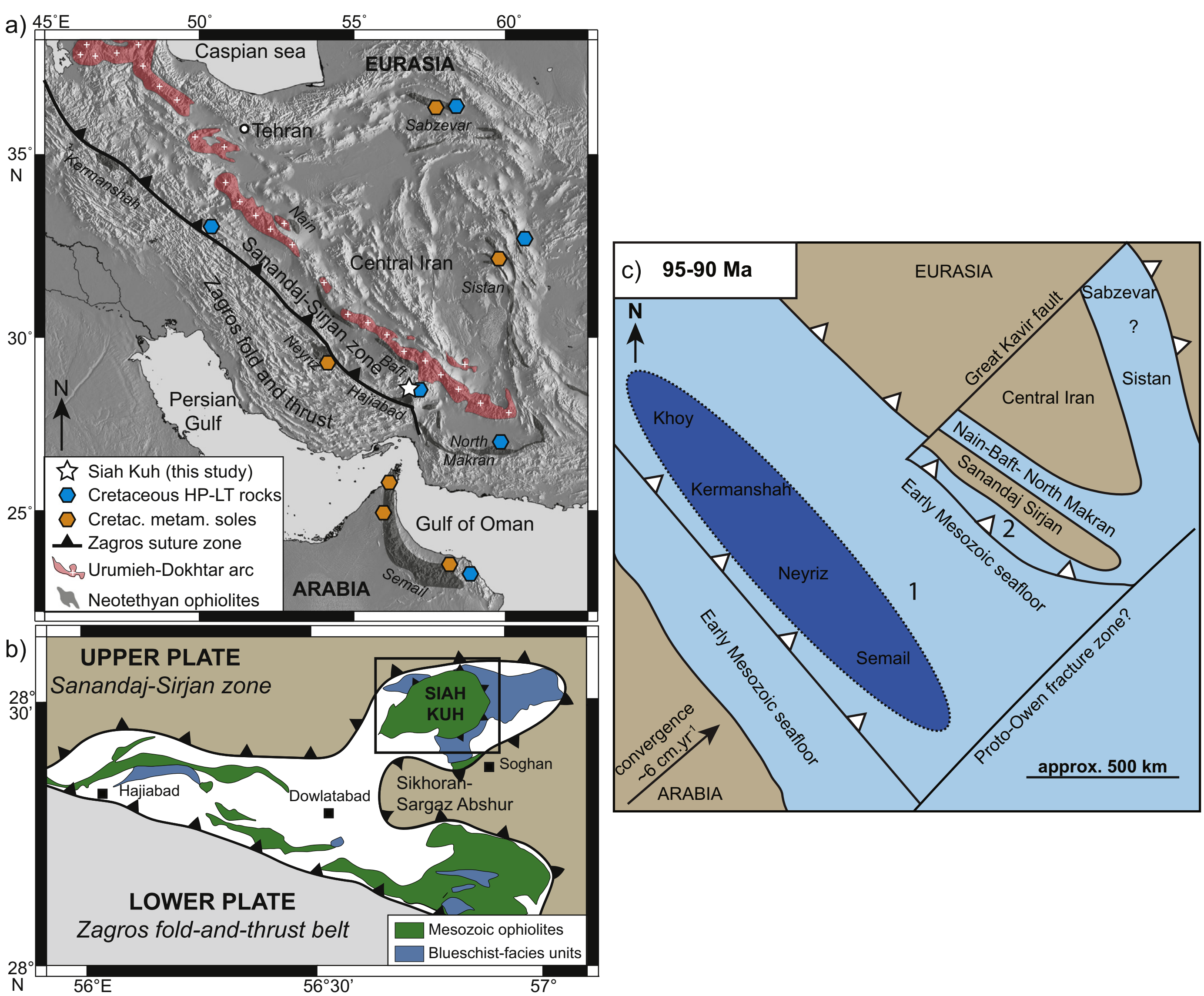

Fig. 1. Geological context. a) Mesozoic and Cenozoic ophiolites and volcanic arcs along the Zagros suture zone; b) Detailed zoom of the Hajiabad-Esfandagheh zone, showing the location of the Siah Kuh unit; c) Paleogeographic map of the Iranian-Omanese Neotethys during Late Cretaceous. Numbers 1 and 2 indicate two hypotheses for the former location of the Siah Kuh seamount (see discussion for more details).

ophiolite) and in Iran along two ophiolite belts: the Outer and Inner Zagros/Makran ophiolite belts (McCall, 1997; Stöcklin, 1981; Fig. 1a).

In the Zagros, the Outer ophiolite belt, located along the Main Zagros Thrust (MZT) includes the (relatively coherent) ophiolitic massifs of Khoy, Kermanshah, Neyriz and Hajiabad-Esfandagheh (from Northwest to Southeast). The Hajiabad (Esfandagheh) ophiolitic exposures (Fig. 1b) are associated with the only blueschist exposures in the Zagros, which led Agard et al. (2006) to interpret the MZT as the Zagros Suture Zone. Dismembered pieces of ophiolites are also found all along the MZT in the so-called "colored mélange" (Gansser, 1960).

All Zagros ophiolites display a large age spread (except the Neyriz ophiolite, where only Late Cretaceous magmatism was described; Babaie et al., 2006; Lanphere and Pamić, 1983; Monsef et al., 2018a), suggesting different stages of magmatic activity, notably during the Triassic-Liassic and Late Cretaceous to Paleocene periods (Ao et al., 2016; Moghadam et al., 2013b, 2017; Whitechurch et al., 2013). The Triassic-Liassic magmatism usually shows alkaline to MORB signatures, whereas the Late Cretaceous one shows an SSZ signature (Ali et al., 2012; Babaie et al., 2001; Khalatbari-Jafari et al., 2004; Moghadam et al., 2013b, 2014b; Saccani et al., 2013; Whitechurch et al., 2013).

The Sanandaj-Sirjan Zone, to the North of the Zagros Suture Zone, is interpreted as a piece of the Eurasian upper plate (e.g. Agard et al., 2011; Ghasemi and Talbot, 2006) that separates the Outer Zagros ophiolite belt from the Inner Zagros ophiolite belt. This belt comprises small dismembered ophiolitic massifs including the Nain, Dehshir, Shahr-e Babak and Baft locations from Northwest to Southeast (abbreviated hereafter as "Nain-Baft"). The magmatism within these units has strong SSZ signatures (Moghadam et al., 2009) and occurred from 'mid' Cretaceous to early Paleocene (Arvin and Robinson, 1994; Moghadam et al., 2013a, 2013c, 2010). Most authors separate the Outer and Inner ophiolite belts, the former being a forearc of a northward-dipping subduction zone (responsible for the Zagros blueschists), the latter being the coeval back-arc (e.g. Agard et al., 2011; Arvin and Robinson, 1994; Moghadam et al., 2009), although some have proposed that both ophiolitic belts belong to the same ophiolite (e.g. Moghadam et al., 2010).

McCall (1997) proposed a continuity between the Zagros and the Makran ophiolites. The Outer ("Colored Mélange") and Inner ophiolite belts are separated by the Bajgan-Durkan complex, analogous to the Sanandaj-Sirjan zone. Cretaceous blueschist facies ophiolitic units of the North Makran suture are however located to the north and structurally above all of these units (Hunziker et al., 2017) and suggest a slightly different geological evolution than in the Zagros. In spite of the scarcity of intact ophiolitic exposures in the continuity of the Outer ophiolite belt, the study of dismembered ophiolites allowed the identification of Late Cretaceous (possibly starting during Early Cretaceous) magmatism with dominant SSZ and accessory MORB signatures (Saccani et al., 2018). Ophiolites in the Inner Makran ophiolite belt, including the Band-e Zeyarat/Dar-e Anar, Ganj, Rameshk-Mokhtarabad, Fannuj-Maskutan, Kahiri-Espakeh and Iranshahr ophiolitic massifs testify to

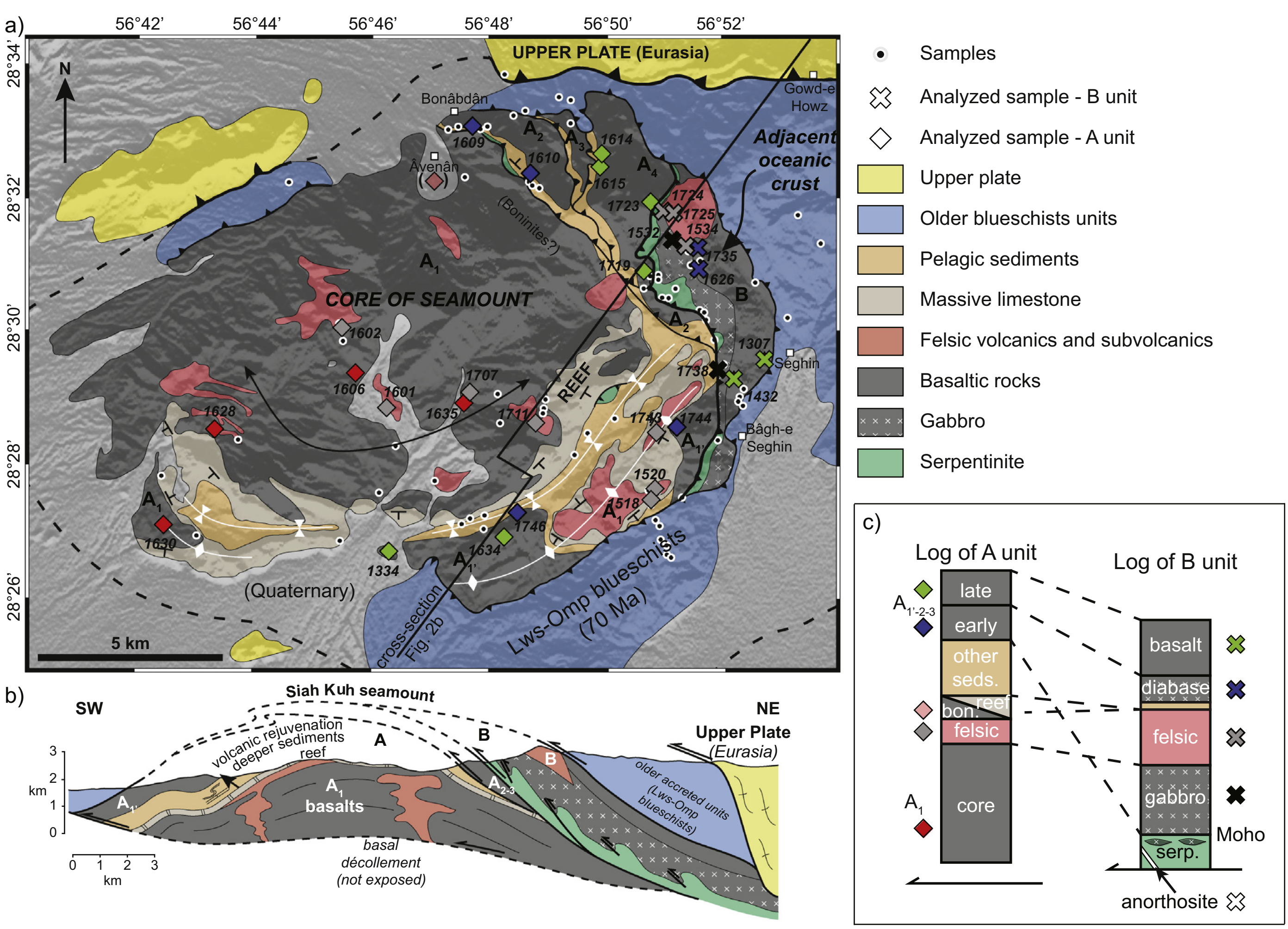

Fig. 2. Structural frame: the Siah Kuh seamount (modified after Bonnet et al., 2019a, 2019b). a) Map of the Siah Kuh unit, the meaning of the color fill for samples is shown in panel c; b) Synthetic cross-section of the Siah Kuh seamount; c) Synthetic log of the A and B units, and proposed correlations (bon. = boninites).

an Early Cretaceous magmatic stage, associated with alkaline (OIB) magmatism, and Late Cretaceous SSZ magmatism (Burg, 2018; Ghazi et al., 2004; Kananian et al., 2001; Monsef et al., 2018b).

Across the Gulf of Oman, the Semail ophiolite is commonly regarded as having formed during the Late Cretaceous (96–94 Ma; Goodenough et al., 2010; Rioux et al., 2013, 2012; Warren et al., 2005), in a SSZ context with increasing maturity, yet never reaching a mature arc stage (Alabaster et al., 1982; Godard et al., 2003).

Given the variety of Late Cretaceous ophiolitic remnants from the Neotethys, linking them to a specific geodynamic context may prove difficult (see the schematic paleogeographical map on Fig. 1c). Exceptional pieces of oceanic lithosphere like the Siah Kuh seamount may help constraining the paleogeography of the Iran-Oman transect, with critical inference for regional-scale geodynamics.

2.2. The Siah Kuh massif, an exhumed seamount

The Siah Kuh unit is a 18 × 12 kilometer-wide and >1.5 km-high coherent portion of ocean floor (Fig. 2a, b) belonging to the Hajiabad ophiolite, close to the transition between Zagros and Makran. At variance to earlier map reports ("colored mélange", Azizan et al., 2007; Madjidi et al., 1993; Nazemzadeh et al., 2007), this unit is a coherent magmatic unit with some sediments and subordinate serpentinite only. It is tectonically overlain by blueschist facies units metamorphosed during Late Cretaceous (Agard et al., 2006; Angiboust et al., 2016; Moghadam et al., 2017; Monié and Agard, 2009; Sabzehei, 1974) and by rocks of the Sanandaj-Sirjan zone, locally represented by the Sikhoran ultramafic-mafic complex (itself capped by metasediments of the Sargaz-Abshur unit, Ahmadipour et al., 2003; Ghasemi et al., 2002). The so-called Siah Kuh granitoids (Arvin et al., 2007) dated to 200 Ma, are located to the North and thrust upon the Siah Kuh unit of this paper, but are not part of it.

The architecture of the Siah Kuh unit is summed up on Fig. 2 (after Bonnet et al., 2019a, 2019b). The Siah Kuh unit is separated into two sub-units (A and B) by a major, km-scale thrust. The A unit is characterized by a magmatic core (A_1) stratigraphically overlain by reef limestone and pelagic sediments, upon which new lavas are erupted (Figs. 2c and 3a, b).

The core of the A unit (A_1) is made of pillow basalts (Fig. 3c) and breccias, intruded by felsic magmatic rocks (Fig. 3d). Moghadam et al. (2013b) reported boninite lavas in this part of the Siah Kuh unit (although the location of these samples is approximate – near the Avenân village, see Fig. 2a – they are unambiguously within and close to the top of the A_1 unit). The felsic intrusions are associated with rhyo-dacitic lava flows on top of the basalts.

The lava flows of the core A_1 unit are stratigraphically overlain by up to 400 m of deepening-up oceanic sediments (Fig. 3a, b, d). The basal sediment is reef to lagoon-like with remains of foraminifera, urchin spines and gastropods (Bonnet et al., 2019a), but is locally absent. Deeper sediments constituted of tuffaceous sandstone, clays, radiolarite and pelagic limestone are deposited above this shallow limestone, all of which are locally infiltrated by felsic sub-volcanic material. These sediments are assumed to be of Campanian to Maastrichtian age in former studies (84–66 Ma; Sabzehei, 1974).

Up to 1 km-thick pillow basalts and basaltic flows (units $A_{1'}$-A_2-A_3-A_4 of Fig. 2a) have been erupted directly on top of the sediments (Fig. 3a, b). While the contact between the A_1 unit and $A_{1'}$-A_2-A_3-A_4 was very often reworked by faults parallel to the sedimentary layer, the original unfaulted, stratigraphic contact is preserved in some places (such as between A_1 and $A_{1'}$, Fig. 2a). This large volume of lavas, marking the resumption of volcanic activity after some period of magmatic inactivity, is described as a "rejuvenation event" in Bonnet et al. (2019a, 2019b). We later separate this rejuvenation event in "early-stage rejuvenation" for the lavas located just above the sediments and "late-stage" for lavas higher in the sequence. As pointed out by Bonnet et al. (2019a, 2019b), the A unit as a whole has all the characteristics of a seamount (i.e. a bathymetric anomaly on the seafloor).

The second sub-unit (Unit B) has a serpentinized ultramafic base intruded by an anorthosite dike (Fig. 3e) and rodingite pods. A large volume of gabbro overlies the ultramafics, with fining-upwards grain size. A 300 m-thick body of felsic volcanics overlain by a thin and very discontinuous layer of pelagic sediments is intercalated in coarse-grained gabbros and diabase (Fig. 3f). In the southern part of the B unit, gabbros are overlain by basalts. The abundance of felsic rocks (rare in ophiolitic rocks from adjacent areas) and sedimentary intercalations that can be correlated with the structure of the A unit suggest that this unit could be a lateral equivalent of the seamount core.

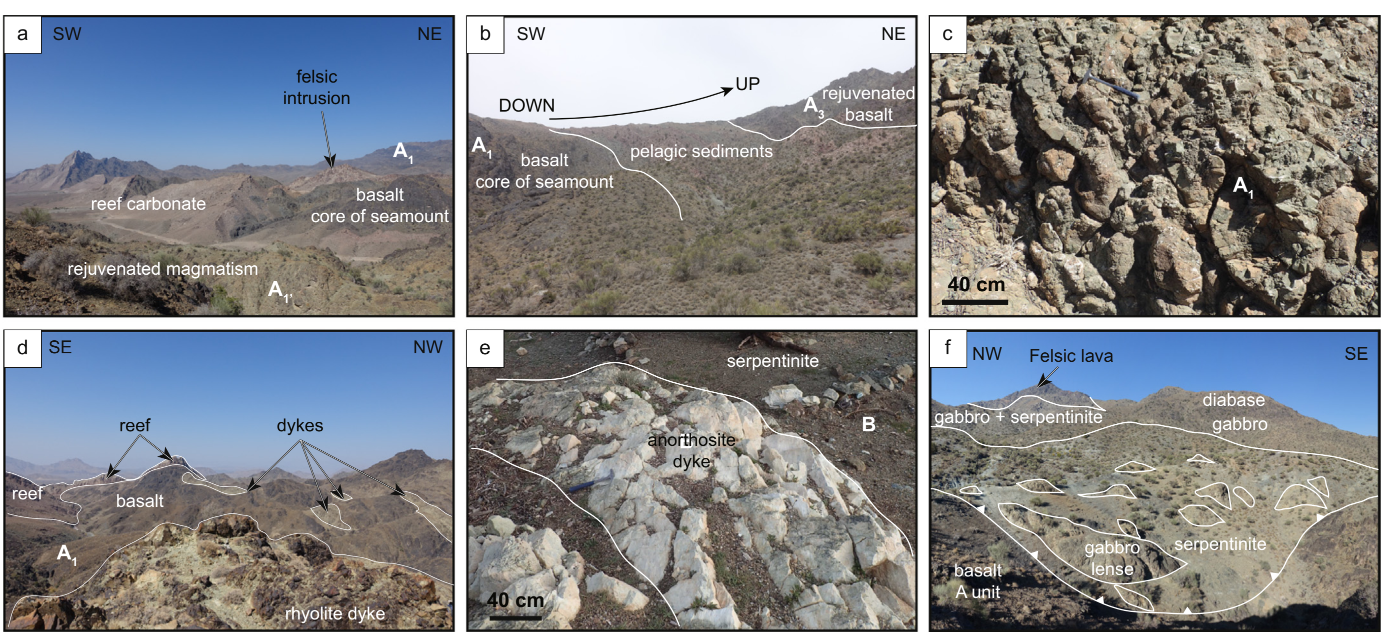

Fig. 3. Field pictures. a) Reef carbonates resting on top of A_1 unit lavas. The granite intrusion is related to felsic lavas studied hereafter. Rejuvenated magmatism of the $A_{1'}$ unit above the limestones; b) Sediment intercalation between the A_1 unit and magmatic rejuvenation in the A unit (A_3); c) Pillow lavas of the core of the seamount; d) Rhyolite dykes in basalt in the core of the seamount (A_1 unit); e) Anorthosite dyke intruding serpentinite at the base of the B unit; f) Structure of the northern B unit.

The whole Siah Kuh seamount was then subducted to ~30 km depth, as attested by very incipient high-pressure metamorphism marked by lawsonite and aragonite crystallization (e.g. Fig. 4d, e). It was subsequently exhumed as an intact piece, with limited subduction-related deformation (these aspects, beyond the scope of the present study, are detailed in Bonnet et al., 2019a, 2019b).

3. Sampling and analytical methods

Approximately 100 samples of magmatic rocks and serpentinized ultramafics were collected in different units of Siah Kuh, including the core of the seamount, the early and late stages of the magmatic rejuvenation, gabbros, diabase and basalt of the B unit, as well as felsic volcanics and subvolcanics. After examination of thin sections, 36 samples were selected for detailed analyses (Table 1). The precise GPS location of each sample is given in Supplementary Material S1.

An aliquot of each magmatic sample (31 samples) was crushed and powdered for 30 min with an electric mortar in agate to avoid contamination. These samples were finely crushed to <2 μm grains for major, trace and Sr-Nd isotopes analyses. About 4 g of each sample was dried at 110 °C in an alumina crucible and heated twice for 1 h to 1000 °C and reweighted for loss on ignition calculation.

Major elements analyses were performed at ALIPP6 (Sorbonne Université) by ICP-OES spectroscopy (with an Agilent 5100 SVDV ICP-OES) after dissolution at 80 °C with HNO_3 and HF and neutralization with $B(OH)_3$. Trace element analyses were also performed at ALIPP6 (Sorbonne Université) through QQQ-ICP-MS spectroscopy (using an Agilent 8800 ICP-QQQ-MS) after dissolution at 80 °C with HNO_3 and HF and neutralization with HNO_3 and H_3BO_3.

Detailed analyses are provided in Supplementary Material S2. Geochemical data were normalized to the primitive mantle values and chondrite values (Sun and McDonough, 1989).

12 samples were selected for bulk rock Sr-Nd isotopic analyses (performed at SARM, Nancy). εNd_i and $^{87}Sr/^{86}Sr(t)$ values were calculated on the basis of their expected ages (Supplementary Material S3). These corrections change the εNd and $^{87}Sr/^{86}Sr$ values by a maximum of 0.7 and 0.00001, respectively.

Clinopyroxene and spinel compositions of 10 basaltic samples and 5 serpentinites have been analyzed using a Cameca SX100 electron microprobe (15 kV, 10 nA, 1 μm spot, WDS) at CAMPARIS (Sorbonne Université), with diopside (Si, Ca, Mg), orthoclase (K, Al), $MnTiO_3$ (Mn, Ti), Fe_2O_3 (Fe) and albite (Na) as standards. The analyses were sorted and Fe^{3+} concentrations were estimated using the method exposed by Droop (1987). Analyses are provided in Supplementary Materials S4 and S5.

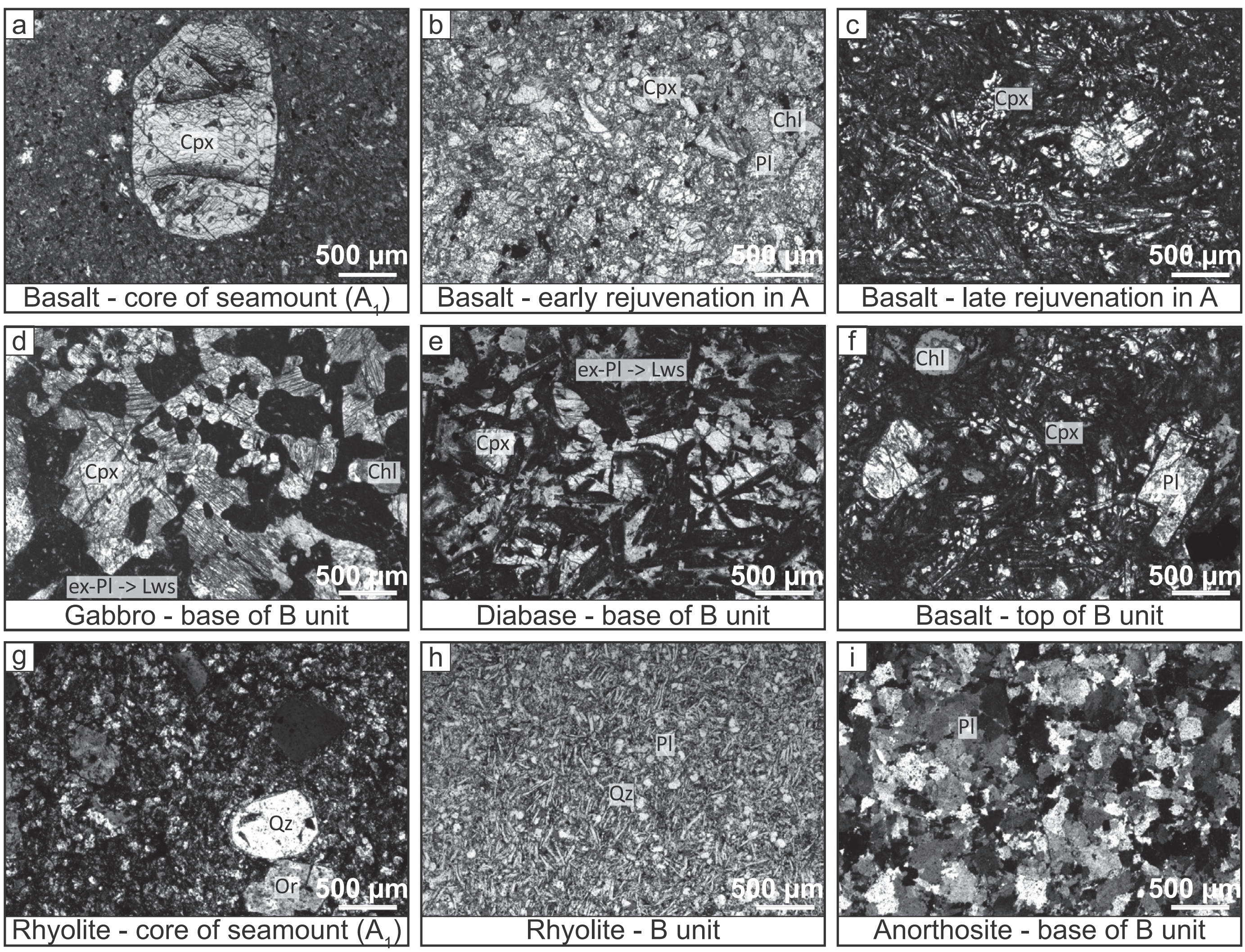

Fig. 4. Microphotographs of representative rocks from the Siah Kuh seamount, from Unit A (a–c), Unit B (d–f) and felsic associated rocks from both units (g–i). All pictures are at the same scale and the white horizontal bar represents 500 μm. a) Porphyric texture of sample 1635; b) Sample 1746 with a phaneritic texture; c) Porphyric texture of sample 1614b; d) Poikilitic texture of sample 1532, where zircons have been dated; e) Intergranular texture of sample 1735; f) Porphyric texture of sample 1432 where zircons have been dated; g) Porphyric texture of sample 1601; h) Trachytic texture of sample 1725; i) Phaneritic texture of sample 1720, where zircons have been dated. Abbreviations are: Cpx: clinopyroxene, Pl: plagioclase, Chl: chlorite, ex-Pl → Lws: replacement of magmatic plagioclase by metamorphic lawsonite, Or: orthoclase, Qz: quartz.

Table 1
Sample nature, performed analyses and detailed mineralogy. Abbreviations are: Cpx: clinopyroxene, Spl: spinel, Pl: plagioclase, Or: orthoclase, Qz: quartz, Gl: glass, Ox: oxide, Cal: calcite, Chl: chlorite, Ep: epidote, Pmp: pumpellyite, Prh: prehnite, Amp: amphibole, Srp: serpentine, Lws: lawsonite, Arg: aragonite.

#	Description	Classification	Analyses					Primary						Secondary (alteration)									High P.		
			Trace	Sr-Nd	Cpx	Spl	U-Pb	Cpx	Pl	Or	Qz	Gl.	Ox	Cal	Qz	Chl	Ep	Pmp	Prh	Amp	Srp	Lws	Arg	Amp
1606	Pillow basalt	A1 mafic	x	x	x			x	x			x	x	x	x	x	x							
1628	Basalt	A1 mafic	x					x	x			x	x	x	x			x					x	
1630	Pillow basalt	A1 mafic	x		x			x	x			x	x	x	x		x	x	x					
1635	Basalt	A1 mafic	x	x	x			ex	x			x	x		x	x								
1518	Rhyolite	A1 felsic	x	x			x			x	x	x	x	x				x				x	x	
1520	Rhyolite	A1 felsic	x							x	x	x	x	x				x						
1601	Granitic rock	A1 felsic	x	x					x	x	x		x			x	x	x						
1602	Granitic rock	A1 felsic	x						x	x	x		x		x		x							
1707	Granitic rock	A1 felsic	x						x	x	x		x			x	x							
1711	Rhyolite	A1 felsic	x							x	x	x	x			x		x						
1743	Rhyolite	A1 felsic	x							ex	x	x	x			x								
1609	Basalt	A early rej.	x						x			x	x	x	x	x				x			x	
1610	Basalt	A early rej.	x	x					x			x	x	x	x			x					x	
1744	Basalt	A early rej.	x						x			x	x				x							
1746	Basalt	A early rej.	x	x	x			x	x			x	x			x								
1334	Basalt	A late rej.	x					No thin section																
1614	Basalt	A late rej.	x		x			x	x			x	x		x	x		x						
1615	Pillow basalt	A late rej.	x						x			x	x	x	x			x						
1634	Pillow basalt	A late rej.	x	x				x	x			x	x		x	x		x					x	
1719	Basalt	A late rej.	x						x			x	x	x	x	x								
1723	Basalt	A late rej.	x	x	x			x				x	x			x								
1626	Diabase	B diabase	x	x	x			x	x			x	x			x								
1735	Diabase	B diabase	x		x			x	x				x		x	x						x		
1307	Basalt	B top	x					No thin section																
1432	Basalt	B top	x	x	x		x	x	x			x	x		x	x								
1534	Dacite	B felsic	x	x					x		x	x	x		x	x		x						
1724	Andesite	B felsic	x						x		x		x				x							
1725	Andesite	B felsic	x						x		x		x			x	x							
1532	Gabbro	B gabbro	x		x		x	x	x				x			x		x		x	x	x		x
1738	Gabbro	B gabbro	x					x	x				x		x	x		x		x		x		x
1720	Plagiogranite	B	x				x		x															
1608	Serp. peridotite	A				x							Spl								x			
1533	Serp. peridotite	B				x							Spl								x			
1622	Serp. chromite pod	B				x							Spl								x			
1535	Serp. peridotite	B				x							Spl								x			
1639	Serp. peridotite	B				x							Spl								x			

Four samples were coarsely crushed and zircon grains were separated for U-Pb dating and Hf isotope analysis, using conventional heavy fraction and magnetic techniques. Zircon grains were placed on epoxy mounts and then polished to expose their half-sections, which were photographed under transmitted and reflected light using an optical microscope to reveal internal cracks and mineral inclusions. Cathodoluminescence (CL) images of the zircon grains were generated using a LEO1450VP scanning electron microscope (SEM) with an attached Gatan MinCL detector at IGGCAS (Supplementary Material S6).

U-Pb dating and trace element analysis of zircons from 4 samples were simultaneously conducted by LA-ICP-MS at the Wuhan SampleSolution Analytical Technology Co., Ltd., Wuhan, China. Detailed operating conditions for the laser ablation system and the ICP-MS instrument and data reduction are the same as description by Zong et al. (2017). Laser sampling was performed using a GeolasPro laser ablation system that consists of a COMPexPro 102 ArF excimer laser (wavelength of 193 nm and maximum energy of 200 mJ) and a MicroLas optical system, with a spot size of 32 μm. An Agilent 7700e ICP-MS instrument was used to acquire ion-signal intensities. Helium was applied as a carrier gas. Argon was used as the make-up gas and mixed with the carrier gas via a T-connector before entering the ICP. A "wire" signal smoothing device is included in this laser ablation system (Hu et al., 2012). Zircon 91500 and glass NIST610 were used as external standards for U-Pb dating and trace element calibration, respectively. Each analysis incorporated a background acquisition of approximately 20–30 s followed by 50 s of data acquisition from the sample. An Excel-based software ICPMSDataCal was used to perform off-line selection and integration of background and analyzed signals, time-drift correction and quantitative calibration for trace element analysis and U-Pb dating (Liu et al., 2010, 2008). Common-Pb correction was done using the method of Andersen (2002). Data reduction was carried out using the Isoplot/Ex v. 2.49 programs (Ludwig, 2001). Analyses of reference zircon Plešovice as an unknown give an accurate date within uncertainty (338.4 ± 1.9 Ma, compared to 337.13 ± 0.37; Sláma et al., 2008). U-Pb and trace element analyses of zircons are provided in Supplementary Material S7, S8 and S9.

In-situ zircon Lu-Hf isotopic analyses were carried out using a Neptune MC-ICP-MS with an ArF excimer laser ablation system. Hf isotopic analyses were obtained on the same zircon grains that were previously analyzed for LA-ICP-MS U-Pb isotopes, with ablation pits of 32–65 μm in diameter and a laser repetition rate of 10 Hz with 100 mJ was used. Details of the technique are described by Wu et al. (2006). Decay constant by Söderlund et al. (2004) and present-day chondritic ratios by Bouvier et al. (2008) were adopted to calculate εHf(t) values. The single stage model age (T_{DM}) was calculated by using the present-day depleted mantle isotopic ratios (Supplementary Material S10, Vervoort and Blichert-Toft, 1999).

4. Petrography

A summary of the mineralogical assemblages is provided in Table 1. We report on Fig. 4 pictures of representative textures from mafic rocks in A (Fig. 4a–c), in B (Fig. 4d–f) and felsic rocks in A (Fig. 4g) and B (Fig. 4h, i).

4.1. Mafic lavas

Mafic lavas are the main constituent of unit A and of the top of B (Fig. 2). They are all basaltic, with clinopyroxene, plagioclase and Fe-Ti oxides in a glassy matrix (Fig. 4a–c, f). Most samples show evidence of hydrothermal alteration, marked by the growth of secondary phases. Pumpellyite, epidote and chlorite usually replace primary clinopyroxene and volcanic glass, while primary plagioclase is often albitized. Quartz, calcite, epidote, prehnite, and pumpellyite fill vesicles and veins that result from strong degassing of magmas during eruption (e.g. Fig. 4f). Green amphibole is found in one basalt. Clinopyroxene phenocrysts are more frequent in the A_1 unit, but generally units cannot be distinguished solely based on magmatic textures.

A few samples show crystallization of high-pressure minerals during subduction, such as lawsonite and pumpellyite replacing plagioclase in one sample, or more frequently aragonite-bearing veins (see Bonnet et al., 2019a, 2019b for more details).

4.2. Gabbros and diabase

Gabbroic rocks are found within the B unit. They are mainly made of plagioclase surrounded by clinopyroxene, with oxide and rare olivine. One sample (#1532) was recovered in a sequence with strong grain size variations (potentially cumulitic). Poikilitic textures are observed in the zones of smaller grain size (Fig. 4d). Hydrothermal minerals include amphibole and chlorite replacing clinopyroxene and serpentine replacing rare olivine. High-pressure metamorphism is common in these samples with lawsonite and pumpellyite replacing plagioclase (Fig. 4d, e).

4.3. Felsic lavas

Felsic lavas in A are mainly rhyolites, with large hexagonal quartz crystals, crystals of orthoclase and oxides in a glassy matrix (Fig. 4g). K-feldspar and glass are usually altered to pumpellyite, epidote and chlorite. One rhyolite also contains aragonite and lawsonite in veins.

Felsic lavas in B are dacitic, with abundant plagioclase, quartz and oxides in a glassy matrix (Fig. 4e). Plagioclase is albitized and the glass is altered to epidote and chlorite during hydrothermalism.

4.4. Felsic intrusives

Felsic intrusives are observed within the A units. They are composed of quartz, plagioclase and K-feldspar. They are characterized by the crystallization of secondary epidote, possibly replacing unidentified primary phases.

4.5. Anorthosite

One anorthosite dyke (#1720) was found in serpentinized ultramafics at the base of the B unit. It is composed of 95% plagioclase, 4% titanite and contains some zircons (Fig. 4i).

4.6. Ultramafic material

Ultramafics are found within both the A and B units, and are close to 100% serpentinized (chrysotile-lizardite, except for spinel that is generally preserved). One sample of serpentinized ultramafics from the A unit is likely a former dunite with two generations of Al-Cr-rich spinel distinguished by their color.

By contrast, ultramafics of the B unit more likely represents a former harzburgite or a cumulate ultramafic sequence, with little-deformed patches of former olivines, and abundant bastite replacing former pyroxene, whose cleavage is revealed by Fe-Ti oxides. A chromitite pod within the ultramafics of the B unit is made of 90% of Cr-spinel and 10% serpentine.

Spinel is the main aluminium-bearing phase in all ultramafic samples. All samples also have secondary magnetite crystallization around serpentinized olivine domains.

5. Bulk rock geochemistry

The whole Siah Kuh volcanic sequence has been affected by hydrothermal alteration, as shown by the widespread occurrence of secondary phases such as chlorite and pumpellyite (e.g. Fig. 4f). This is further evidenced by addition of H_2O, as attested by the 0.9 to 8.5 wt% loss on ignition of the rocks (the loss on ignition may in part correspond to CO_2 loss, from minor secondary carbonate vesicles). To avoid any bias due to major element mobilization during hydrothermal alteration and/or high-pressure metamorphism, we only present diagrams based on elements assumed to be immobile (see discussion in Section 9.1). Immobile-element-based classifications of mafic rocks are shown on Fig. 5, trace element spectra on Fig. 6 and trace-element based discrimination diagrams on Fig. 7.

5.1. Core of the seamount (A_1)

Mafic rocks from the core of the seamount plot in the subalkaline basaltic field in the Zr/Ti – Nb/Y diagram (Pearce, 1996; Fig. 5a) and in the tholeiitic basalt to andesite fields in the Th – Co diagram (Hastie et al., 2007; Fig. 5b). REE diagrams (Fig. 6a) show low LREE content compared to MREE and HREE (with very low REE contents for two samples: <5*chondrite for LREE and <8*chondrite for HREE). These rocks have

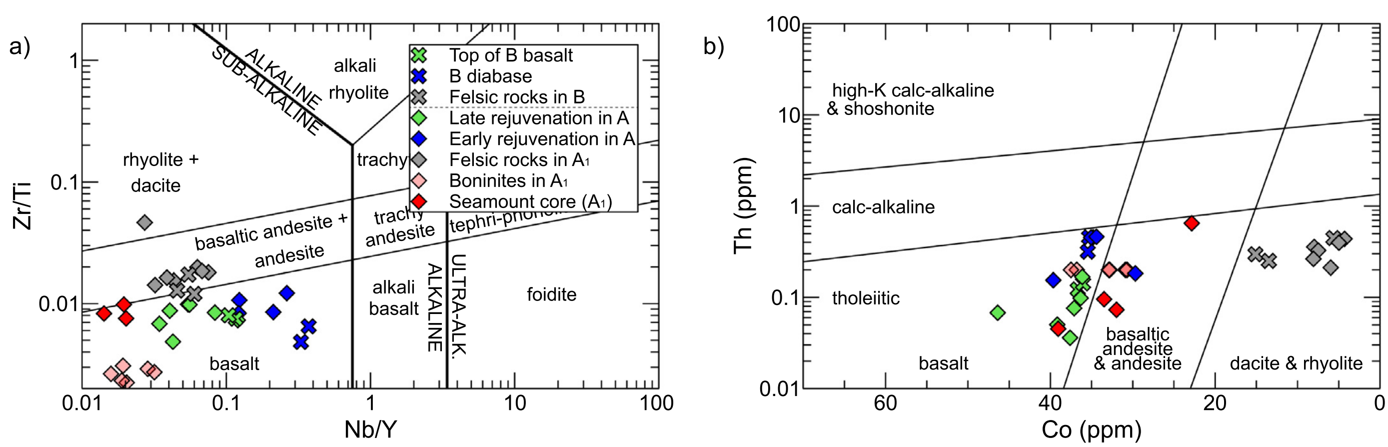

Fig. 5. Classification of rocks based on immobile elements. a) Zr/Ti – Nb/Y diagram after Pearce (1996); b) Th – Co diagram after Hastie et al. (2007). Siah Kuh boninites after Moghadam et al. (2013b).

trace element signatures very similar to the lower V2 lavas from Oman (Alabaster et al., 1982; Godard et al., 2003; Kusano et al., 2014). Multielementary spider diagrams (Fig. 6b) show strong Nb-Ta negative anomalies, and small Ti negative anomalies. They plot in the IAT field on the Th/Yb – Nb/Yb (Pearce, 2008; Fig. 7a), in the arc field of the V – Ti diagram (Shervais, 1982; Fig. 7b) and in the IAT and calc-alkaline fields of the Th – Hf – Ta diagram (Wood, 1980; Fig. 7c). They range between MORB and arc basalts in the Th/La – Sm/La diagram (Plank, 2005; Fig. 7d). One sample (#1628) shows Th and LREE enrichment and plots in or close to the calc-alkaline field of the former diagrams.

5.2. Boninites

Boninites from the core of Siah Kuh were not analyzed in this study, but we herein report bulk-rock analyses by Moghadam et al. (2013b). They are classified as subalkaline basalts in Fig. 5a, and as tholeiitic basalts to andesites in Fig. 5b. REE diagrams show strong depletion in LREE compared to HREE (Fig. 6a). They are chemically very close to Oman boninites (upper V2, Ishikawa et al., 2005, 2002; Kusano et al., 2014). They plot in the IAT field in Fig. 7a and in the boninite field in Fig. 7b.

5.3. Felsic rocks

Felsic rocks plot in the subalkaline basaltic andesite/andesite field in Fig. 5a, except for one sample in the dacite/rhyolite field (despite being petrographically dacites and rhyolites or subvolcanic equivalents) and in the tholeiitic dacite/rhyolite field in Fig. 5b. No obvious difference exists between the felsic rocks of the A_1 unit and those of the B unit (apart from a smaller Ti negative anomaly in the latter). They have flat to slightly decreasing REE patterns, with marked negative Eu anomaly (Fig. 6c). Multi-elementary spider diagrams show strong Nb-Ta and Ti negative anomalies, and small Zr negative anomalies (Fig. 6d). They also plot in the IAT fields in Fig. 7a and c (except for one sample plotting in the calc-alkaline field; the use of those diagrams is however contested for felsic rocks; Pearce, 2008). They mainly plot as arc lavas in the Th/La – Sm/La diagrams, with higher Th/La ratios than other rocks.

5.4. Early stage rejuvenation (A unit: $A_{1'}$ and A_2)

Lavas from the early rejuvenation stage plot as subalkaline in Fig. 5a, and as tholeiitic basalts in Fig. 5b. They are enriched in LREE compared to HREE (Fig. 6e). Multi-elementary spider diagrams show no significant HFSE negative anomaly (Fig. 6f). They plot in-between E-MORB and N-MORB in Fig. 7a, and in the MORB – back-arc basalt field in Fig. 7b. They are in the E-to-N-MORB transition zone of Fig. 7c, and are classified as MORB in Fig. 7d.

5.5. Late stage rejuvenation (A unit: $A_{1'}$ and A_4)

Rocks from the late stage rejuvenated magmatism are classified as subalkaline basalts in Fig. 5a and as tholeiitic basalts to andesites in Fig. 5b. They have bell-shaped REE patterns with depletion in LREE and slight depletion in HREE compared to MREE (Fig. 6e). Multi-elementary spider diagrams show very small Nb-Ta and Ti negative anomalies (Fig. 6f). They plot close to N-MORB in Fig. 7a and in the MORB – back-arc basalt field of Fig. 7b. They are classified as N-MORB in Fig. 7c, and as MORB (yet closer to the OIB field the early-stage rejuvenation lavas) in Fig. 7d.

5.6. B unit diabases

Samples from the base of the B unit are classified as subalkaline in Fig. 5a and as tholeiitic basalts in Fig. 5b. They are enriched in LREE, but have almost flat MREE-HREE trend (Fig. 6g). Multi-elementary spider diagrams show small positive Nb-Ta anomalies but strong negative Zr-Hf anomalies (Fig. 6h). They plot very close to E-MORB in Fig. 7a and in the MORB-BABB field of Fig. 7b. They plot in the E-MORB to OIB basalt transition in Figs. 6, 7c and d.

5.7. B unit basalts

Basalts from the top of the B unit are classified as subalkaline basalts in Fig. 5a and as tholeiitic basalts in Fig. 5b. They have again a flat, slightly bell-shaped REE patterns with a small enrichment in MREE compared to LREE and HREE (Fig. 6g). Multi-elementary spider diagrams show an insignificant negative Ti anomaly (Fig. 6h). They plot in-between the N-and-E-MORB fields of Fig. 7a and c, in the MORB-BABB field of Fig. 7b, and in the MORB field of Fig. 7d.

5.8. Anorthosite

Its REE pattern has high LREE to HREE ratio and a strong positive Eu anomaly, characteristic of plagioclase (Fig. 6c). Multi-elementary spider diagrams show Zr-Hf and Ti negative anomalies (Fig. 6d).

5.9. Gabbros of the B unit

Two gabbros within the B unit show very distinct geochemical signatures (Fig. 6g, h). One (#1738) has a REE profile very similar to the diabase of the B unit, with similar positive Nb-Ta positive anomalies and Zr-Hf negative anomalies but with a positive Ti anomaly. The other one (#1532, dated) has enriched MREE and HREE compared to LREE, with a positive Eu anomaly and small negative Ti anomaly. The later resembles the N-MORB-like basalts from the top of the B unit, but is more depleted, probably due to cumulative effects.

6. Radiogenic (Sr and Nd) isotope analyses

Representative samples from all extrusive sequences presented above have been analyzed for Sr-Nd isotopes. Results are presented on Fig. 8.

All samples are relatively clustered in εNd_i with positive values between 6.68 and 9.21. $^{87}Sr/^{86}Sr(t)$ is relatively more dispersed with values between 0.7045 and 0.7063. All rocks plot out of the mantle correlation line (Fig. 8). There is a progression from high $^{87}Sr/^{86}Sr(t)$ values (around 0.7063) for the core of the seamount to lower values in the felsic rocks (around 0.7055–0.706), and even lower values for the rejuvenation event in A and in the mafic rocks of the B unit (between 0.7045 and 0.7055). Isotopic data on the Siah Kuh lavas are comparable with data from other regional ophiolites (Fig. 8; Oman: Godard et al., 2006; Neyriz: Moghadam et al., 2014b; Nain-Baft: Moghadam et al., 2013c).

7. Mineral chemistry

Bulk-rock analyses might be affected by hydrothermal alteration on the seafloor. Consequently, compositions of unaltered clinopyroxenes and spinels in the rocks were measured as they may yield direct information on the magmatic source. Compositional plots for clinopyroxene are shown on Fig. 9a, b, c (after Leterrier et al., 1982) and for spinel on Fig. 9d (after Dick and Bullen, 1984). Detailed analyses of clinopyroxene and spinel are available in the Supplementary Materials S1 and S2.

7.1. Core of the seamount (A_1)

Clinopyroxenes have low Ca + Na between 0.75 and 0.9 atoms per formula unit (apfu), low Ti content (<0.015 apfu) which place them in the tholeiitic to calc-alkaline basalt field of Fig. 9a, usually low Ti + Cr (average at 0.01 apfu) and high Ca (0.7–0.9 apfu) placing them in the orogenic basalt field of Fig. 9b. Due to their low Ti content, they plot in the island arc tholeiite field of Fig. 9c.

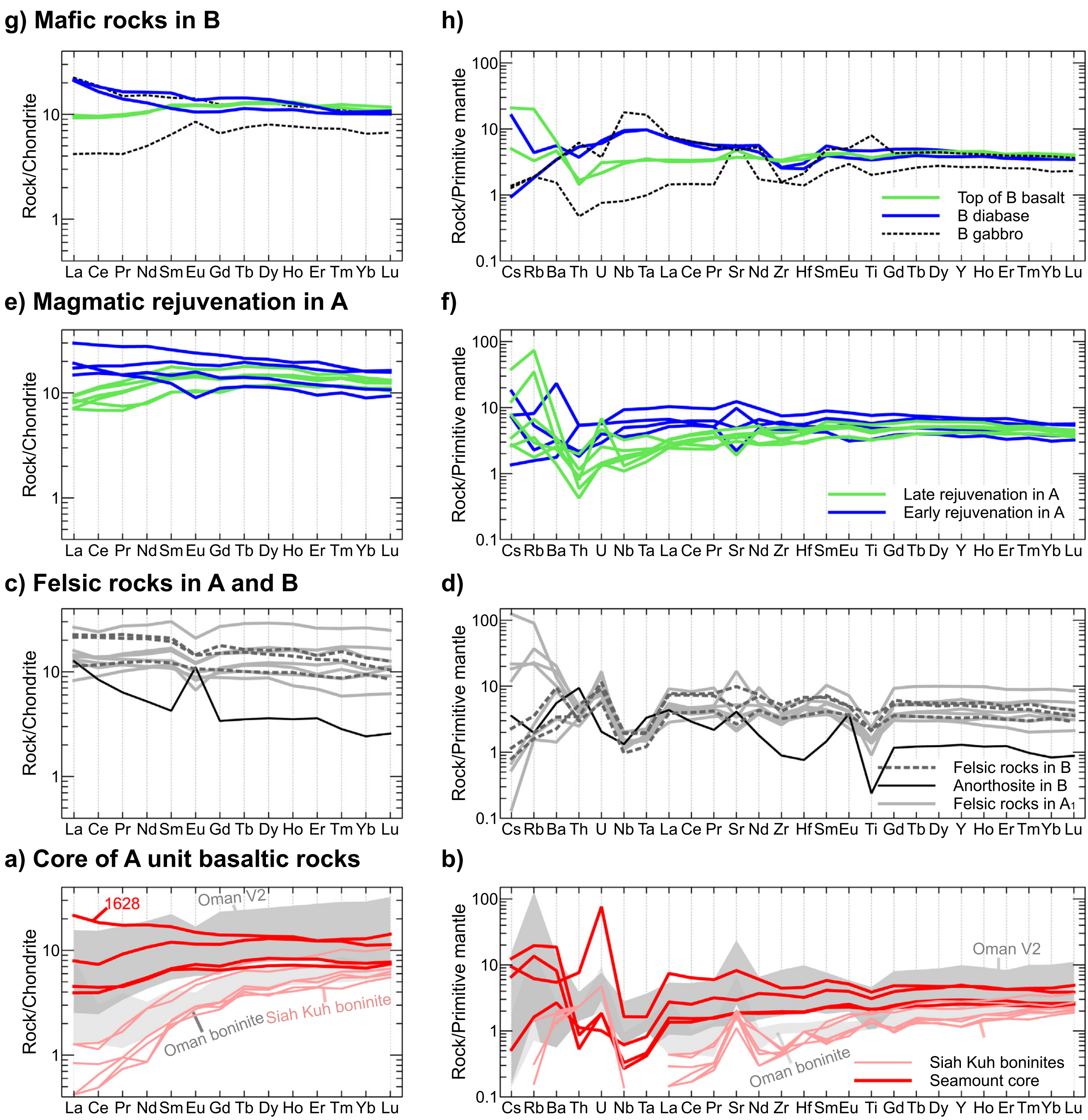

Fig. 6. Rare-earth element and multi-element diagrams for all rocks normalized to chondrite and primitive mantle respectively (Sun and McDonough, 1989). (a, b) Mafic rocks of the core of the A unit; (c, d) Felsic rocks of the A and B units; (e, f) Magmatic rejuvenation within the A unit; (g, h) Mafic rocks of B unit, including Siah Kuh boninites (Moghadam et al., 2013b). Reference spectra are Oman V2 (Alabaster et al., 1982; Godard et al., 2003) and Oman boninite (Upper V2, Ishikawa et al., 2005; Kusano et al., 2014).

7.2. Early rejuvenation in A

Clinopyroxenes have higher Ti concentration of 0.02–0.04 apfu and low Ca + Na around 0.5–0.8 apfu, high Ti + Cr (0.02–0.035 apfu), which place them in the mid-ocean ridge tholeiite field of Fig. 9a and b.

7.3. Late rejuvenation in A

Clinopyroxenes have low Ca + Na concentration of 0.7–0.9 apfu, placing them in the subalkaline field, and high Ti + Cr of 0.02–0.05 apfu placing them in the mid-ocean ridge tholeiite field of Fig. 9a and b.

7.4. B unit gabbro

Clinopyroxenes from sample 1532 have Ca + Na concentrations between 0.85 and 0.92 apfu, placing them mostly in the subalkaline field (Fig. 9a), and high Ti + Cr of 0.03–0.035 apfu placing them in the mid-ocean ridge tholeiite field in Fig. 9b.

7.5. B unit diabase

Clinopyroxenes have low Ca + Na concentration between 0.7 and 0.8 apfu, placing them in the subalkaline field (Fig. 9a), and high Ti + Cr

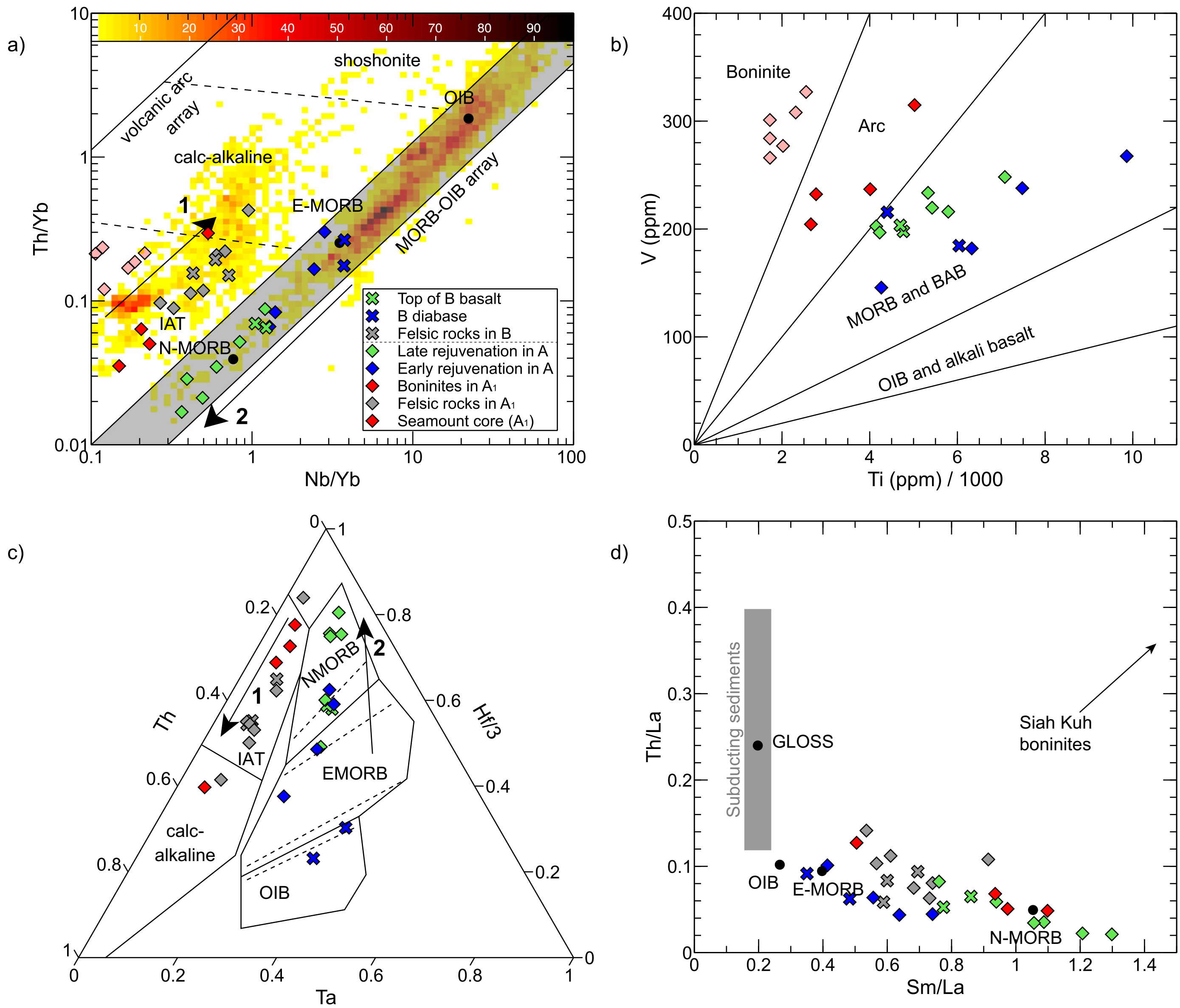

Fig. 7. Trace element discrimination diagrams of mafic rocks. a) Th/Yb vs Nb/Yb diagram by Pearce (2008), with a density map of the composition of basalts from present-day seamounts (including intra-oceanic arc seamounts). GLOSS (global subducting sediment) values from (Plank and Langmuir, 1998) The scale refers to the number of occurrence in the Georoc database (http://georoc.mpch-mainz.gwdg.de); b) V vs Ti diagram by Shervais (1982); c) Th-Hf-Ta ternary diagram by Wood (1980); d) Th/La vs Sm/La diagram after Plank (2005). Siah Kuh boninites after Moghadam et al. (2013b).

of 0.02–0.045 apfu placing them in the mid-ocean ridge tholeiite field in Fig. 9b.

7.6. B unit basalt

Clinopyroxene has 0.75–0.85 apfu Ca + Na, placing them in the subalkaline field (Fig. 9a), and high Ti + Cr of 0.02–0.04 apfu placing them in the mid-ocean ridge tholeiite field (Fig. 9b).

7.7. Spinel in ultramafic rocks

Two generations of spinels have been analyzed in an ultramafic rock from A, with similar lobate (magmatic) textures yet no textural relationships (Fig. 9d, Supplementary Material S5). One has Cr# of 0.44–0.54, Mg# of 0.60–0.66 and Ti < 0.0018 apfu, while the other has higher Cr# of 0.69–0.75, Mg# of 0.50–0.55 and Ti of 0.0010–0.0032 apfu. The first generation plots in the overlap between the abyssal and supra-subduction fields, while the second generation has clear supra-subduction signatures (Fig. 9d). Spinels in ultramafics from B have a wide range of Ti concentrations (0.002–0.025 apfu), a likely indicator of a cumulative origin. The Ti content increases toward the top of the ultramafic sequence. The lowermost spinels compare with the first generation of the A unit, with similar Cr# (0.46–0.52) but slightly lower Mg# (0.66–0.7).

8. Zircon U-Pb dating and Hf isotope analyses

Zircons have been separated from four different kinds of rocks, belonging to the A unit (#1518, rhyolite) and the B unit (#1720, anorthosite; 1532, gabbro; 1432, basalt). Zircons are abundant in anorthosite and gabbro, but scarce in rhyolite and basalt. Most of them have clear magmatic textures (Supplementary Material S3). Only concordant zircons were considered. Zircon cathodoluminescence images, trace element analyses and trace element diagrams are available in the Supplementary Materials S3, S4 and S5 respectively.

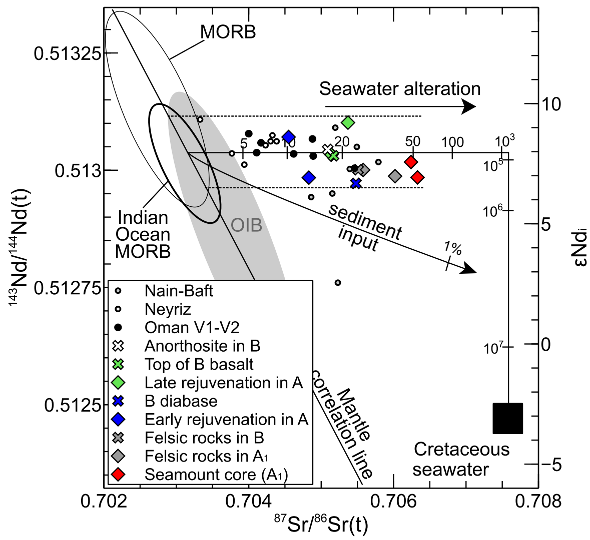

Fig. 8. Sr-Nd isotope values for representative rocks of each unit. Cretaceous seawater-rock mixing line from McCulloch et al. (1981), mixing curve with GLOSS sediment from Plank and Langmuir (1998). Oman data from Godard et al. (2006), Neyriz from Moghadam et al. (2014b) and Nain-Baft from Moghadam et al. (2013c).

8.1. Rhyolite in A

Despite the small number of zircons in the rock, five concordant zircons show strong inheritance with ages scattered between 1800 and 87 Ma (Fig. 10a). The youngest zircon population (n = 2) defines a maximum age with a weighted average of 87.0 ± 1.8 Ma. These two zircons have positive εHf around 10, and T_{DM} ages around 500 Ma (Fig. 11).

8.2. Gabbro in B

Thirteen concordant zircons yield a weighted average age of 77.8 ± 0.98 Ma (Fig. 10b). Single ^{238}U-^{206}Pb ages are scattered between 81 and 75 Ma. All the zircons have very positive εHf values around 14 and T_{DM} ages around 270 Ma (Fig. 11).

8.3. Anorthosite in B

Fourteen concordant zircons yield a weighted average age of 77.3 ± 1.5 Ma (Fig. 10c). Single ^{238}U-^{206}Pb ages are scattered between and 82 and 73 Ma. Most of these zircons have positive εHf values around 9 and T_{DM} ages around 540 Ma (Fig. 11).

8.4. B unit basalt

Despite the small number of zircons in the rock, five concordant zircons show strong inheritance with ages scattered between 500 and 73 Ma (Fig. 10d). The youngest zircon population (n = 2) defines a

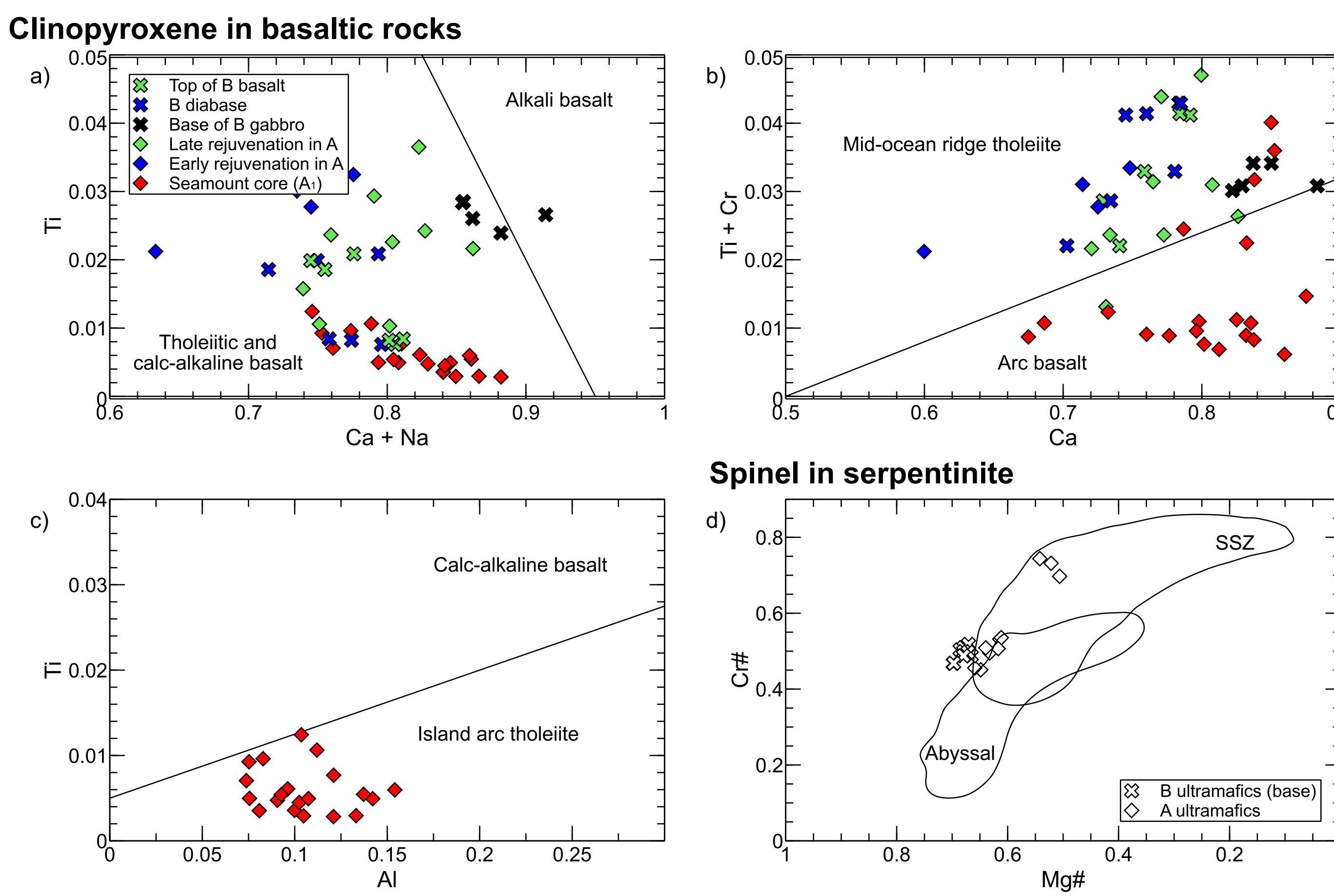

Fig. 9. Mineral compositions of clinopyroxene and spinel. (a-c) Clinopyroxene discrimination diagrams in mafic rocks from Leterrier et al. (1982). a) Ti vs Ca + Na diagram showing all clinopyroxenes plotting in the calk-alkaline to tholeiitic field; b) Ti + Cr vs Ca diagram showing most of the clinopyroxene analyses from the core of the seamount plotting in the orogenic basalts field and other mafic rocks in the non-orogenic tholeiite field; c) Ti vs Al diagram showing that clinopyroxenes from the core of the seamount plot in the arc tholeiite field (other analyses not plotted); d) Cr# vs Mg# diagram for spinel in ultramafic rocks after (Dick and Bullen, 1984) showing all analyses plotting in the supra-subduction zone field.

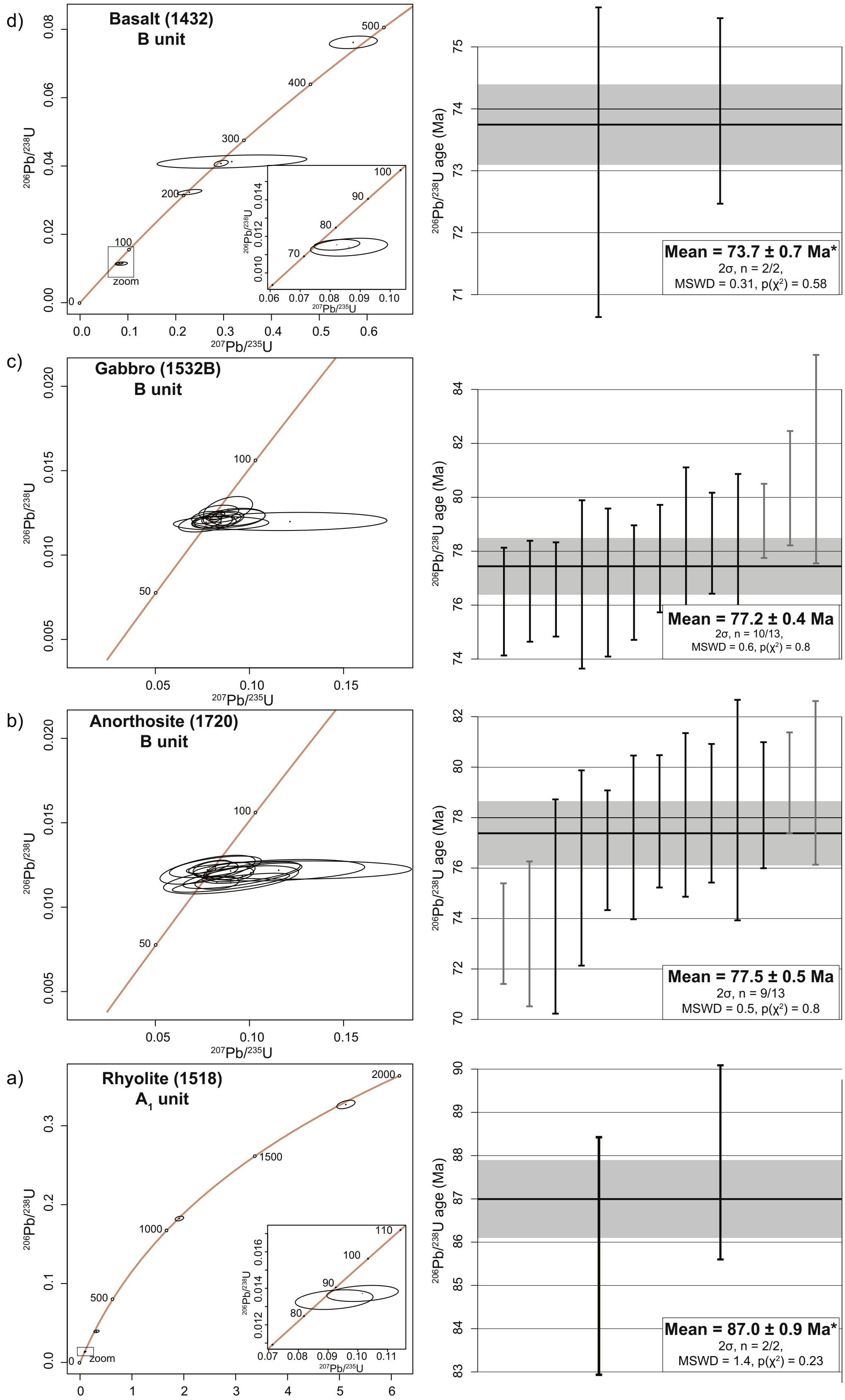

Fig. 10. Wetherill Concordia diagrams for 4 samples and $^{206}Pb/^{238}U$ age dispersion plots. a) Rhyolite within A1 (sample 1518), inset shows a zoom on the 70–110 Ma age window; b) Anorthosite within B (sample 1720); c) Gabbro within B (sample 1532); d) Basalt at the top of B (sample 1432), inset shows a zoom on the 70–110 Ma age window. Ages mentioned are weighted averages (*: youngest zircon population).

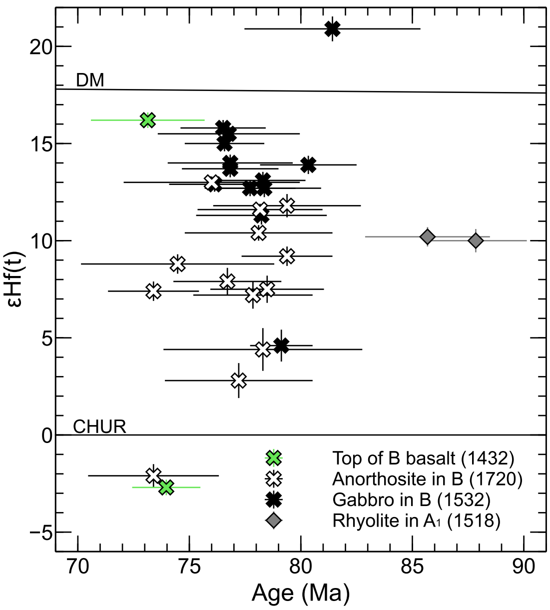

Fig. 11. Zircon εHf(t) vs age plot showing positive values for most zircons.

maximum age for this basalt with a weighted average of 73.7 ± 1.3 Ma, with very distinct εHf values of −3 and 16 (Fig. 11).

9. Discussion

9.1. Effects of seafloor alteration and metamorphism

Seafloor alteration and metamorphism can modify significantly the chemical composition of ophiolitic rocks. Major elements can vary a lot through intense hydration of rocks (represented by LOI, from 0.9 to 8.6 wt%). Here, most of the hydration occurs at the seafloor, as attested by the appearance of chlorite, epidote and pumpellyite (e.g. Fig. 4d, f). Examining correlations between the amount of volatiles in the rock (LOI) and major and trace-elements concentrations (Humphris and Thompson, 1978) can help decipher alteration effects in the rock. In the studied samples Si and Na are inversely correlated with the LOI, even when not considering felsic rocks that are usually much less hydrated than basalts (Supplementary Materials S6). Bulk rock major elements such as Si, Na, K, Ca and trace elements including Cs, Rb, Ba, Sr (LILE) are modified by seafloor alteration (Frey and Weis, 1995; Gillis, 1995), questioning the relevance of the TAS and AFM diagrams for altered oceanic rocks. Relict clinopyroxenes are likely trustworthy indicators of the chemistry of the magma, as they are primary minerals with a composition that is governed at first order by the partition coefficients of elements with the magma (Leterrier et al., 1982). Destabilization or recrystallization of clinopyroxene is harder than that of plagioclase (e.g. Spilde et al., 1993).

Instead, most high field strength elements (HFSEs), and rare earth elements (REEs) are generally considered to be immobile during alteration (e.g. Cann, 1970). Rock classification based on immobile elements should however be used with care, and cannot replace a careful petrographic examination, as rhyolites in our study were misclassified as andesites in the Zr/Ti – Nb/Y. Trace element ratios used in discrimination diagrams as well Sr, $^{87}Sr/^{86}Sr(t)$, Nd and εNd_i values show no correlation with LOI (Suppl. Material S11). Seawater alteration is however commonly cited as one of the main factors affecting $^{87}Sr/^{86}Sr$ signatures of altered lavas (Hauff et al., 2003; Kawahata et al., 2001). A careful examination of the Sr isotopic signatures shows a negative correlation between the Sr or REE and $^{87}Sr/^{86}Sr$ (Suppl. Material S12), trending toward seawater compositions This is best explained by a relatively stronger effect of seawater alteration on rocks that initially contain little Sr, i.e. the most depleted rocks.

Incipient blueschist metamorphism of the whole Siah Kuh unit (at ~200–250 °C, 0.6–0.9 GPa) should also be considered as it is associated with fluid circulation (Bonnet et al., 2019a, 2019b). However, rocks never fully equilibrate at these conditions making the metamorphic imprint very limited (and restricted to some magmatic rocks of the B unit). Associated fluid circulations at T < 300 °C make alteration during metamorphism less likely than alteration at the seafloor. Further we only discuss the petrogenesis based on alleged immobile elements.

9.2. Evolution of geochemical signatures and tectonomagmatic setting

The Siah Kuh seamount is the ideal place to study the evolution of the magmatic source of an ophiolite: unlike most ophiolitic “mélanges” or large-scale ophiolites (save the Oman ophiolite), the structural framework as well as relative and absolute magmatic chronologies are well-constrained here. Furthermore, the Siah Kuh seamount records the evolution of lava chemistry in a single area, so that variations through time may reflect either mantle heterogeneities, viscous flow and/or chemical changes of the composition through time (i.e., due to melt extraction, fluid circulation or source mixing).

9.2.1. An initial supra-subduction event

The supra-subduction origin of altered magmatic rocks may be reflected by four mostly independent trends in the trace elements: (1) rare-earth elements-depleted melts (due to the melting of an already depleted mantle, König et al., 2010), (2) HFSE (including Ti, Nb, Ta, Zr, Hf) depletion compared to REE elements (due to trapping by refractory phases such as Fe-Ti oxides; Briqueu et al., 1984; Gao et al., 2007), (3) V enrichment due to oxidizing conditions above subduction zones enhancing the solubility of V (Shervais, 1982), and (4) enrichment of the source in LREE and Th by sediment-derived fluids (including melts, König et al., 2010; Plank, 2005). The contamination of the source by sediment-derived melts also leads to a strong decrease of εNd toward sedimentary values (around −8, Plank and Langmuir, 1998; e.g. Kusano et al., 2017). These trends are variably observed in the rocks from the A_1 unit (core of the seamount) and in the felsic rocks of B.

The lowermost basalts in A_1 are slightly depleted in rare-earth elements (Fig. 6a), in HFSE (Nb-Ta and small Ti negative anomalies, Figs. 6b and 7a, b, c), but do not show enrichment in Th or V (except for one sample, #1628, that is higher in the sequence; Fig. 7a, d). These signatures are typical of arc tholeiites. Clinopyroxene compositions from the A_1 basalts also show sub-alkaline signatures and are comparable to IAT clinopyroxenes (Fig. 9). Sr-Nd isotopes have clustered values of εNd (6.93–7.57), yet variable Sr isotopic ratios (0.70551–0.70633; Fig. 8). The high εNd values preclude any significant contribution from sediments melts to the mantle source. High $^{87}Sr/^{86}Sr$ values are best explained by hydrothermal alteration of the basalts (Suppl. Material S12), as is commonly expected for altered oceanic rocks (e.g. Godard et al., 2006; Hauff et al., 2003; Kawahata et al., 2001).

Felsic rocks from A and B have uniform chemical compositions, with a strong depletion in HFSE (Figs. 6d, 7a, c) and small enrichment in Th (Fig. 7a, d). εNd values (6.98–7.25) are comparable to those of the basalts.

Boninites show a strong depletion in rare earth elements (Fig. 6a) and Ti (Fig. 7b), but enrichment in Th and V (Fig. 7a, b). There are no Nd isotope measurements on these rocks.

There are no clues for high-pressure melting of slab lithologies (i.e. in the garnet stability field, which would result in HREE-depleted adakitic magmas; e.g. Martin, 1999).

This set of data advocates for several partial melting events of a metasomatized supra-subduction mantle source, with limited contamination by sediment-derived melts (at least for the arc tholeiites and felsic rocks, likely involving more sediments in the boninites; Haase et al., 2015; Ishikawa et al., 2005; Kusano et al., 2017). Hence the A_1

(core) unit of the Siah Kuh seamount and the felsic rocks in the B unit represents the magmatic evolution of an intraoceanic arc from an IAT to IAT/calc-alkaline-transitional felsic rocks and boninites. This evolution is similar to what is currently recorded in intraoceanic arc systems, notably at the initiation of subduction (e.g. Belgrano and Diamond, 2019; Hawkins et al., 1984; Pearce et al., 1984; Stern and Bloomer, 1992).

Concordant zircons have been analyzed in a rhyolite from this event. They show a broad range of ages (1823–85.7 Ma), but the youngest population (2 zircons) was dated at 87.0 ± 0.9 Ma, and is a plausible age for eruption, given the Campanian-Maastrichtian age of overlying sediments proposed by Sabzehei (1974). The lowermost basalts (core of A unit basaltic rocks) upon which this rhyolite was erupted should be somewhat older. Xenocrystic zircons might originate from sediment melts possibly contaminating the mantle source (although the contribution of sediment melts to the source of these rocks is very limited), or they were more likely assimilated from the sub-arc crust during eruption.

9.2.2. A MORB rejuvenation event

In sharp contrast with the A_1 unit, lavas erupted above sediments (i.e. in the $A_{1'}$-A_2-A_3-A_4 and B units) show no strong depletion in rare-earth elements (Fig. 6e), very limited-to-absent HFSE negative anomalies (Fig. 6f) and no Th enrichment (Fig. 7a, d), i.e. no supra-subduction signatures. They are in fact clustered in two trends (with some internal variability): the early stage lavas show an E-MORB-like signature while the late stage is characteristic of N-MORB (Figs. 6e, f and 7). A similar trend is observed in mafic rocks of the B unit (Fig. 6g, h), which is thus likely to be a lateral equivalent of A, as suggested by the spatial association and the correlation of lithologies. Clinopyroxene analyses confirm their mid-ocean ridge tholeiitic signature (Fig. 9). The positive εNd of basalts (6.83 to 9.21; Fig. 8) is compatible with a moderately depleted mantle source (Patchett, 1983). E-MORB and N-MORB lavas are generated in modern oceans at mid-ocean ridges (Michael, 1995; Niu et al., 1999) and in back-arc spreading centers (e.g. Stern et al., 1990). In the latter configuration, the subduction signature is very variable, but its absence may be characteristic of a large distance from the subduction and/or influence from a more primitive mantle (e.g. Lau Basin, Volpe et al., 1988; Mariana back-arc, Pearce et al., 2005).

Anorthosite and gabbro in the B unit are two favorable lithologies for zircon dating. Both rocks have similar ages within uncertainty around 77–78 Ma. The dated gabbro (#1532) has REE and trace element profiles similar to N-MORB, and no obvious HFSE negative anomalies (Fig. 6g, h). Its textural characteristics, reminiscent of cumulates (i.e. similar to some observed on the Mid-Atlantic ridge, Tiezzi and Scott, 1980; depletion in REE and Eu positive anomaly, Seifert et al., 1996), make it unsuitable for discrimination diagrams of Fig. 7. Clinopyroxene analyses plot in the mid-ocean ridge tholeiite field (Fig. 9). This suggests that this gabbro has a (likely N-) MORB affinity. An attempt to date zircons in basalts from top of the B unit yielded a broad range of ages (1080–73.1 Ma), with a youngest population (two zircons) giving a plausible eruption age of 73.7 ± 0.7 Ma that must be cautiously interpreted. These Late Cretaceous ages are consistent with the relative chronology and the mapped Upper Cretaceous sediments.

These data reveal a multistage magmatic history for the Siah Kuh seamount, which evolved from arc tholeiite and boninite to calc-alkaline-transitional possibly until ~87 Ma, and later experienced a distinct magmatic episode of E-to-N-MORB affinity, starting around 77.5 Ma and possibly lasting until 73 Ma (Figs. 7a, 10).

9.3. Constraints on the nature and evolution of the underlying mantle

Mantle rocks found in the Siah Kuh unit are mainly serpentinized dunites (A unit) and cumulates (B unit). The high Cr# of spinels are characteristic of a depleted mantle (Dick and Bullen, 1984; Moll et al., 2007). However, a second generation of Cr-richer spinel in a dunite of the A unit might have formed by impregnation of the mantle by boninitic melts during island arc volcanism (e.g. Barnes and Roeder, 2001).

The restricted spread of the εNd_i values across all magmatic rocks analyzed suggest the melting of a mantle source without a significant contribution from sediment melts (<1%), in particular during the arc stage, when it is most expected (e.g. Zamboni et al., 2016). This signature might however exist in boninites (not analyzed for Nd isotopes) that show a significant Th enrichment. Hence, εNd_i values around 6–10 likely reflect the composition of a slightly heterogeneous mantle that was not strongly contaminated by sediments during the subduction responsible for arc formation. These values are very similar to those of other regional ophiolites (Oman, Godard et al., 2006; Neyriz, Moghadam et al., 2014b; Nain-Baft, Moghadam et al., 2013c), and are comparable with the abnormal modern Indian Ocean MORB (likely refertilized by old subductions; Dupré and Allègre, 1983; Xu and Castillo, 2004). εHf(t) values of zircons are in majority positive (2 values are negative), around 14 for gabbro and 9 for plagiogranite, which points to partially-depleted mantle sources with some heterogeneity.

The evolution from supra-subduction to MORB signatures is opposite to what is observed in many other ophiolites (e.g. Oman, Godard et al., 2003, Albania, Dilek et al., 2008), commonly explained by progressive contamination of the mantle by subduction-derived fluids and melts (occurring in ~1 My, Rioux et al., 2013). Instead, our observations are reminiscent of longer-term processes (~10 My) occurring in modern arc-back-arc systems, such as the Marianas: while the arc itself has a strong supra-subduction signature, back-arc lavas only show a limited subduction component, due to the upwelling of uncontaminated mantle (Pearce et al., 2005). The dissipation of the subduction signature could also be explained by the end of subduction and the replacement of the underlying mantle facilitated by fast horizontal asthenospheric flow (e.g. Faccenna et al., 2014).

The transition from E-MORB to N-MORB lavas (Fig. 10) during the rejuvenation event might be linked with (1) initial heterogeneity of the mantle, (2) a progressive depletion of an initially enriched mantle source due to melt extraction, or (3) changes in the fusion rate of a depleted mantle source. E-MORB lavas are usually thought to stem from plume enrichment of the mantle or assimilation of formerly erupted lavas (e.g. Hémond et al., 2006). The generation of N-MORB lavas could then result from a progressive depletion of this mantle wedge due to melt extraction. An alternative way to form N-MORB lavas after E-MORB basalts from the same depleted mantle source would merely require an increase of the fusion rate by a few percents. However, this process would not explain the variability of the Nb/Yb and Th/Yb ratios as well as the variability of zircon εHf(t) values and whole rock εNd values, that require some heterogeneity in the underlying mantle. The Late Permian T_{DM} age of zircons in gabbro might relate to the fusion of a mantle depleted during the Late Permian, which corresponds to widespread magmatism on both sides of the Neotethys (potentially plume-related, Ghasemi et al., 2002; Lapierre, 2004). Older (~550 Ma) T_{DM} in the anorthosite could however relate to crustal contamination.

Finally, the presence of old zircons xenocrysts (200 Ma to 1.7 Ga) in Siah Kuh magmatic rocks as well as granitoid xenoliths in the Siah Kuh volcanics (2–3-cm-long angular granitic-to-granodioritic enclaves according to Sabzehei (1974) – though never observed in our study) might reflect the nature of the sub-arc crust, partially assimilated during the ascent of magma, or subducted sediments in the source (although this hypothesis is less likely given the very limited contribution of sediments to the source). The ages of these zircons indeed correspond to magmatic events recorded in the continental margins of the Neotethys (Ahmadipour et al., 2003; Ghasemi et al., 2002; Moghadam et al., 2017).

9.4. Geodynamic reconstructions of the Neotethys realm

The regional record of processes described below is detailed in Table 2.

9.4.1. Initial rifting and early spreading history (Permian to Jurassic)

In the Siah Kuh region, the magmatic history associated with rifting and early spreading of the Neotethys is relatively well preserved in the Sikhoran complex: Late Permian to Late Triassic gabbroic complexes have enriched to depleted tholeiitic signatures, with some crustal contamination (Ahmadipour et al., 2003), and partially intrude the overlying metamorphics. The end of high temperature metamorphism and anatexy of Sargaz-Abshur sediments around 200 Ma (Early Jurassic; Ghasemi et al., 2002) are coeval with the sealing of both igneous and metamorphic rocks by Lower Jurassic unmetamorphosed sediments (Sabzehei, 1974). The Sikhoran complex would thus correspond to a Jurassic Ocean-Continent Transition (e.g. Péron-Pinvidic and Manatschal, 2009) on the Northern Side of the Neotethys. Equivalents would be the Bajgan-Durkan complex and the ultramafic Sorkhband-Rudan massif (Delavari et al., 2016; Hunziker et al., 2015; McCall, 1997). Some of the rifting history is recorded throughout Zagros and in Oman by the association of the Upper Triassic to "Mid"-Cretaceous deep sediments (grabens) and shallow sediments, the latter being described as allochtons or "Exotics" (Gharib and De Wever, 2010; Jannessary and Whitechurch, 2008; Ricou, 1974; Ricou et al., 1977; Searle and Graham, 1982; Wrobel-Daveau et al., 2010). Triassic to Liassic alkaline lavas (Ricou, 1974; Saccani et al., 2013; Searle, 1980; Whitechurch et al., 2013) are precusors to Liassic volcanic sequences with E-MORB affinities (although rarely exposed, e.g. Moghadam et al., 2017, 2013b; Searle, 1980).

9.4.2. Subduction: arc development at the northern margin (Jurassic-Oligocene) and Cretaceous-Paleocene back-arcs

The structure of the Zagros suture zone suggests a strong inheritance from northward subduction of the Neotethys/Arabian Plate below Iran (e.g. Agard et al., 2011), yet the timing of subduction initiation is not well-constrained. Abundant subduction-related magmatism has been associated with this subduction (Berberian and Berberian, 1981; Omrani et al., 2008 and references therein). Although Early to Mid-Jurassic calk-alkaline magmatism (e.g. Jafari et al., 2018; Shahbazi et al., 2010) suggests subduction initiation during the Early Jurassic (see also the compilation of Hassanzadeh and Wernicke, 2016; their Fig. 7), this interpretation is challenged by some authors, who outline that subduction signatures could be related to crustal contamination (Azizi and Stern, 2019; Barbarin, 1999; Hunziker et al., 2015). Instead, these authors propose an inception of subduction during Late Cretaceous, which is however inconsistent with the recovery of 'mid' Cretaceous blueschists made of Neotethyan seafloor in Zagros and Makran (as early as 120 Ma in Zagros, Agard et al., 2006; Moghadam et al., 2017; and 100 Ma in Makran, Delaloye and Desmons, 1980), and with Zagros eclogites possibly formed during Neotethyan subduction (with ages ~185–170 Ma, Davoudian et al., 2008, 2016).

Extension and spreading interpreted as back-arc in the Eurasian upper plate (Nain-Baft, Sistan and Sabzevar basins), which started during Albian/Aptian (~125–100 Ma; Babazadeh and de Wever, 2004; Moghadam et al., 2014a, 2009; Rossetti et al., 2010; Zarrinkoub et al., 2012), also require that subduction started at least during Early Cretaceous.

Arc magmatism was recorded continuously in Southern Iran, in the Sanandaj-Sirjan zone (until the Late Cretaceous; Jafari et al., 2018), the Kermanshah arc (Paleocene-Eocene; Whitechurch et al., 2013), and the Urumieh-Dokhtar magmatic arc (post-Eocene; Omrani et al., 2008).

9.4.3. Late Cretaceous compressional event

A main feature of the Neotethys is the intra-oceanic subduction that started at the end of the Early Cretaceous in various areas (e.g. Oman, Neyriz, Turkey; Table 2), leading to the emplacement of supra-subduction ophiolites and metamorphic soles (e.g. Hacker et al., 1996).

Rocks from the core of the Siah Kuh seamount are very similar to those from the V2 stage in the Semail ophiolite, in particular arc tholeiites and boninites (Alabaster et al., 1982; Belgrano and Diamond, 2019; Godard et al., 2003; Ishikawa et al., 2005). This V2 event, dated between 96.4 and 95.5 Ma (Rioux et al., 2013, 2012) is older than what is dated in Siah Kuh. However, felsic intrusives in the Semail ophiolite have been dated between 90 and 85 Ma (Gnos and Peters, 1993; Lippard et al., 1986; Searle, 1980) and could correspond to the felsic rocks in Siah Kuh. The few My delay between forearc magmatism (arc tholeiites and boninites) in Oman and intra-oceanic arc magmatism (felsic rocks) recorded in Oman (and potentially in the Siah Kuh unit) corresponds to the time required for the transition between forearc and arc signatures (7–8 Myr in the Bonin arc; Ishizuka et al., 2011). The Neyriz and Kermanshah ophiolitic complexes in Zagros potentially record similar processes (Babaie et al., 2006, 2001; Delaloye and Desmons, 1980; Jannessary, 2003; Lanphere and Pamić, 1983; Monsef et al., 2018a; Whitechurch et al., 2013).

Subduction initiation was linked with a compressive event (Agard et al., 2007, 2014) responsible for the exhumation of blueschists all along the Neotethys from Turkey to the Western Himalayas (Monié and Agard, 2009), as well as initiation of subduction within back-arcs (e.g. Sabzevar: Rossetti et al., 2010; Sistan: Bonnet et al., 2018).

While arc magmatism is only subordinate in Oman, the Siah Kuh seamount core (A_1 unit), formed around 87 Ma, may represent the arc products of this southern, intra-oceanic subduction (see further discussion below).

9.4.4. Evidence for a second Late Cretaceous spreading phase

This study reports a Late Cretaceous MORB-type magmatic event in the Neotethys (i.e., B unit and magmatic rejuvenation in A unit). In the Kermanshah ophiolite, a magmatic event at ~79 Ma (Ao et al., 2016) was likely associated with a slow-spreading event (Wrobel-Daveau et al., 2010). E-MORB dykes dated at ~81 and ~76 Ma in the Sikhoran complex (Ahmadipour et al., 2003; Ghasemi et al., 2002) could also correspond to this magmatic event. In comparison, an arc-related magmatic phase is recorded during the Late Cretaceous in the Nain-Baft-North Makran ophiolites (Kananian et al., 2001; Monsef et al., 2018b).

The magmatic evolution observed in the Siah Kuh seamount hints to the change from an arc to back-arc-like setting, and its possible original location in the Neotethys is therefore discussed below.

9.5. Where was the arc?

The Siah Kuh seamount is presently sandwiched within the Zagros suture zone and domed below other exposures of Zagros blueschists and of the Sikhoran complex (e.g. Agard et al., 2006; Angiboust et al., 2016). Although challenged by some authors (e.g. Moghadam and Stern, 2015), there is generally a consensus on the existence of two north-dipping subduction zones within the Neotethys (e.g. Coleman, 1981; Searle and Cox, 1999; Rossetti et al., 2010; Agard et al., 2011): (1) the long-lived North-Neotethys subduction zone initiated during the Jurassic and lasting until Eocene, and (2) the short-lived South Neotethys subduction zone initiated in mid-Cretaceous times and terminated by the Late Cretaceous with the continental subduction of the Arabian platform (Agard et al., 2010; Searle et al., 2004).

Geochemical evidence suggest that Siah Kuh formed in an intraoceanic forearc/arc setting, and later evolved in a back-arc setting. Whether this occurred in the upper plate of subduction (1) or (2) is unclear. We hereafter discuss two different scenarii featured in Fig. 12b and c.

9.5.1. Hypothesis 1: arc of the Southern Intra-Neotethys Subduction

Most of the magmatic activity documented in the Southern Neotethys (e.g. Neyriz, Oman) occurred around 95 Ma (e.g. Monsef et al., 2018a; Rioux et al., 2012; see Table 2). The 87 Ma age recorded within Siah Kuh is approximately 10 Ma younger than supra-subduction magmatism. At this time, the Semail ophiolite underwent a ~140–150° clockwise rotation and recorded alkaline magmatism (Morris et al., 2016; Umino, 2012; van Hinsbergen et al., 2019).

Table 2
Regional analogs of the Siah Kuh massif related to their Neotethyan context: 1: main Neotethys rifting/spreading, 2: North Neotethys subduction, 3: South Neotethys subduction, 4. Late Cretaceous spreading, Kermanshah arc (Whitechurch et al., 2013), Kermanshah ophiolitic complex (Ao et al., 2016; Delaloye and Desmons, 1980; Gharib and De Wever, 2010; Ricou et al., 1977; Saccani et al., 2013; Whitechurch et al., 2013; Wrobel-Daveau et al., 2010), Zagros eclogites (Davoudian et al., 2008, 2016), Neyriz ophiolitic complex (Babaie et al., 2006, 2001; Jannessary, 2003; Jannessary and Whitechurch, 2008; Lanphere and Pamić, 1983; Moghadam et al., 2014b; Monsef et al., 2018a; Ricou, 1974), Siah Kuh unit (Moghadam et al., 2013b, this study), South Hajiabad ophiolite (Moghadam et al., 2017, 2013b), Zagros blueschists (Agard et al., 2006; Angiboust et al., 2016; Moghadam et al., 2017; Monié and Agard, 2009), Sikhoran complex (Ahmadipour et al., 2003; Ghasemi et al., 2002), Sargaz-Abshur complex (Ghasemi et al., 2002; Sabzehei, 1974), Oman Exotics (Searle and Graham, 1982), Haybi complex (Searle, 1980), Semail ophiolite (Alabaster et al., 1982; Godard et al., 2003; Guilmette et al., 2018; Hacker et al., 1996; Ishikawa et al., 2005, 2002; Lachize et al., 1996; Rioux et al., 2016, 2013, 2012; Rollinson, 2015; Soret et al., 2017), Oman blueschists (El Shazly et al., 2001; Searle et al., 2004; Warren et al., 2005; Warren and Waters, 2006; Yamato et al., 2007), Makran colored mélange (Burg, 2018; Saccani et al., 2018), Makran blueschists (Delaloye and Desmons, 1980; Hunziker et al., 2017), Western Iranian Makran (Mohammadi et al., 2017), Nain-Baft ophiolite (Moghadam et al., 2013a, 2009; Pirnia et al., 2019), Sistan ophiolite (Babazadeh and de Wever, 2004; Tirrul et al., 1983; Zarrinkoub et al., 2012), Sabzevar ophiolite (Moghadam et al., 2014a; Rossetti et al., 2014; Kazemi et al., 2019), Sanandaj-Sirjan zone (Arvin et al., 2007; Jafari et al., 2018; Shahbazi et al., 2010), Urumieh-Dokhtar zone (Omrani et al., 2008).

Locality	Type of rock	Age	Possibly represents?	Reference
Kermanshah arc, Western Zagros	Arc volcanism (Kamyaran)	Paleocene-Eocene	2. North Neotethys arc	Whitechurch et al. (2013)
	Bisotun carbonates (shallow sediments)	Upper Triassic-Upper Cretaceous	1. Rifted allochtons	Ricou et al. (1977); Wrobel-Daveau et al. (2010)
	Radiolarite series (deep sediments)	Lower Jurassic-“Mid”-Cretaceous	1. Rifted allochtons	Ricou et al. (1977); Wrobel-Daveau et al. (2010); Gharib and De Wever (2010)
Kermanshah ophiolitic complex (Harsin-Sahneh), Western Zagros	Alkaline lavas	Triassic to Liassic	1. Rifting	Saccani et al. (2013); Whitechurch et al. (2013)
	IAT	86–81 Ma	3. Cretaceous SSZ magmatism	Whitechurch et al. (2013); Delaloye and Desmons (1980)
	Rodingitized gabbro dike in peridotite	79.3 Ma	4. Late Cretaceous spreading?	Ao et al. (2016); Wrobel-Daveau et al. (2010)
Zagros eclogites, Western Zagros	Shahrekord eclogite	185–110 Ma	2. North Neotethys subduction?	Davoudian et al. (2008, 2016)
	Megalodon limestone (shallow sediments)	Upper-Triassic	1. Rifted allochtons	Jannessary and Whitechurch (2008); Ricou (1974)
	Pichakun unit (deep sediments)	Upper Triassic-“Mid”-Cretaceous	1. Rifted allochtons	Jannessary and Whitechurch (2008); Ricou (1974)
	Alkaline lavas	Triassic	1. Rifting	Ricou (1974)
Neyriz ophiolitic complex, Central Zagros	Metamorphic sole	94.9 ± 7.6 Ma	3. South Neotethys subduction	Lanphere and Pamić (1983)
	Arc tholeiite to boninites	100–92 Ma	3. Cretaceous SSZ magmatism	Moghadam et al. (2014b); Babaie et al. (2006); Jannessary (2003); Lanphere and Pamić (1983); Monsef et al. (2018a)
	Calc-alkaline volcanics (Hassanabad unit)	Cretaceous	3. Cretaceous SSZ magmatism	Babaie et al. (2001)
Siah Kuh unit, Eastern Zagros	Arc tholeiites - core of seamount	Before 87 Ma? … 95 Ma?	3. Cretaceous SSZ magmatism	Moghadam et al. (2013b); this study
	Felsic volcanism	87 Ma?	3. Cretaceous SSZ magmatism	This study
	MORB magmatism	78–73 Ma	4. Late Cretaceous spreading	This study
South Hajiabad ophiolite, Eastern Zagros	E-MORB lavas	194–186 Ma	1. Early spreading	Moghadam et al. (2013b); Moghadam et al. (2017)
Zagros blueschists, Eastern Zagros	Ashin blueschists Seghin blueschists	120–60 Ma	2. North Neotethys subduction	Agard et al. (2006); Monié and Agard (2009); Angiboust et al. (2016); Moghadam et al. (2017)
Sikhoran mafic-ultramafic complex, Eastern Zagros	Gabbroic complexes (contaminated MORB)	250–180 Ma	1. Rifting and early spreading	Ghasemi et al. (2002); Ahmadipour et al. (2003)
	Diabasic dykes	160–130 Ma	1. Early spreading	Ghasemi et al. (2002)
	E-MORB diabasic dikes	81–76 Ma	4. Late Cretaceous spreading	Ghasemi et al. (2002); Ahmadipour et al. (2003)
Sargaz-Abshur complex, Eastern Zagros	Unmetamorphosed sediments	~200 Ma	1. Rifting (end)	Sabzehei (1974); Ghasemi et al. (2002)
Oman Exotics, Oman	“Oman exotics” carbonates	Up. Permian to “mid”-Cretaceous	1. Rifted allochtons	Searle and Graham (1982)
Haybi complex, Oman	Alkaline lavas	Triassic	1. Rifting	Searle (1980)
	E-MORB lavas	Triassic	1. Early spreading	Searle (1980)
Semail ophiolite, Oman	Metamorphic sole	105–95 ± 3 Ma	3. South Neotethys subduction	Hacker et al. (1996); Rioux et al. (2016); Soret et al. (2017); Guilmette et al. (2018)
	V2 volcanism (supra-subduction)	96.4–95.5 Ma	3. Cretaceous SSZ	Alabaster et al. (1982); Godard et al. (2003); Ishikawa et al. (2002, 2005); Rioux et al. (2012, 2013)

Table 2 (*continued*)

Locality	Type of rock	Age	Possibly represents?	Reference
			magmatism	
	Calc-alkaline felsic intrusives	90–85?	3. Cretaceous SSZ magmatism	Gnos and Peters (1993); Lippard et al. (1986); Searle (1980); Briqueu et al. (1991); Ishikawa et al. (2005); Lachize et al. (1996); Rollinson (2015)
Oman blueschists	As-Sifah blueschists and eclogites	~80 Ma	3. South Neotethys subduction	El Shazly et al. (2001); Searle et al. (2004); Warren et al. (2005); Warren and Waters (2006); Yamato et al. (2007)
Makran colored mélange	Limestone rafts	Permian to Late Jurassic	1. Rifted allochtons	Burg (2018)
	Alkaline and arc volcanism	~130 Ma and 95–75 Ma	3. Cretaceous SSZ magmatism?	Saccani et al. (2018)
Makran blueschists	Blueschists	~100 Ma	2. North Neotethys subduction	Delaloye and Desmons (1980); Hunziker et al. (2017)
Western Iranian Makran	Detrital zircons in sediments	~105, 95, 85, 76 Ma	2. North Neotethys arc	Mohammadi et al. (2017)
Nain-Baft ophiolite, Northern Zagros	SSZ volcanic rocks	Early Cretaceous-Paleocene	2. North Neotethys back-arc?	Moghadam et al. (2009); Moghadam et al. (2013a); Pirnia et al. (2019)
Sistan ophiolite, E. Iran	MORB to SSZ volcanic rocks	Albian-Paleocene (-Eocene)	2. North Neotethys back-arc	Babazadeh and de Wever (2004); Zarrinkoub et al. (2012); Tirrul et al. (1983)
Sabzevar ophiolite, E. Iran	SSZ volcanic rocks	Aptian-Paleocene (-Eocene)	2. North Neotethys back-arc	Rossetti et al. (2014); Moghadam et al. (2014a); Kazemi et al. (2019); Mazhari et al. (2019)
Sanandaj-Sirjan zone, Northern Zagros	Arc volcanism	Early Jurassic?-Late Cretaceous	2. North Neotethys arc	Arvin et al. (2007); Shahbazi et al. (2010); Jafari et al. (2018)
Urumieh-Dokhtar zone, Northern Zagros	Arc volcanism	Post-Eocene	2. North Neotethys arc	Omrani et al. (2008)

However, subduction had not ended yet (as shown by later subduction and blueschist to eclogite metamorphism of the Arabian margin; e.g. El Shazly et al., 2001; Searle et al., 2004; Yamato et al., 2007) and partial melting may have occurred in the mantle north of the Semail ophiolite (Fig. 12b). Resulting magmas would probably be erupted on early Mesozoic oceanic crust, possibly in the presence of extensional allochtons similar to those of the Sargaz-Abshur complex. The development of an arc system more mature than in Oman (i.e., including true calc-alkaline magmas) could be favored by deeper and stronger hydration of the mantle wedge.

The ~78 Ma event recorded in Siah Kuh corresponds to the time when continental rocks start to be exhumed (El Shazly et al., 2001; Yamato et al., 2007). Resistance to the convergence and subduction of the Arabian platform, combined with the slab pull generated by the deeper oceanic slab could induce slab roll back, possibly followed by slab break off (a deep slab was imaged by van der Meer et al., 2018). This process, modeled by Chemenda et al. (1996), may have generated back-arc extension in the upper plate. An asthenospheric window would also allow the influx of heat as well as enriched mantle that could form the MORB lavas. If the Siah Kuh unit was located in an arc/back-arc of the Southern Neotethys Subduction, it would belong to the lower plate of the Northern Neotethys Subduction and get subducted lately (i.e. close to collision, for example during the late Paleocene-Eocene) along with remnants of the Early Mesozoic seafloor. This hypothesis easily explains its underplating beneath the Ashin and Seghin blueschist facies units (Fig. 12b; Agard et al., 2006; Angiboust et al., 2016).

9.5.2. Hypothesis 2: arc of the Northern Neotethys Subduction?

The present position of the Siah Kuh unit below the other Zagros blueschists (Agard et al., 2006) and sequential accretion outlined by Angiboust et al. (2016) make it difficult to reconcile with a Northern Neotethys subduction zone (see Fig. 12b, c). The main argument for a genesis in this context is a possible genetic link between the Sikhoran-Sargaz-Abshur complexes and the Siah Kuh seamount, as discussed above. No clear arc magmatism at 87 Ma is however described in the obducted ophiolites (Semail-Neyriz) or in the Sanandaj-Sirjan zone surrounding the Siah Kuh unit. Genesis of Siah Kuh above the Northern Neotethys subduction would require the existence of extensional allochtons similar to the Sargaz-Abshur complex (to explain the zircon distribution). Formation above the Northern Neotethys subduction could explain the Late Cretaceous E-MORB dykes within the Sikhoran complex. Arc magmatism in Siah Kuh likely corresponds to a magmatic event recorded in Makran by detrital zircons aged 90–85 Ma, interpreted by Mohammadi et al. (2017) and Burg (2018) to result from arc magmatism on the Northern margin of the Neotethys. However, detrital zircons aged 80–75 Ma are not particularly abundant in these studies.

In this configuration, subduction of the Siah Kuh seamount would require (1) initiation of a new subduction zone to the north of the Northern Tethys Subduction or (2) a northward migration of the subduction zone, for example through a splay fault (dotted line in Fig. 12c). Initiation of a new subduction zone above a pre-existing one is observed in Southeastern Taiwan, where a large portion of the forearc gets subducted (e.g. Malavieille et al., 2002). Boutelier et al. (2003) suggested that subduction initiation would occur preferentially in the back-arc. In this configuration, however, subduction of the largely intact Siah Kuh seamount would require a huge mega-splay fault, much larger than the one observed in the Nankai accretionary wedge (Park et al., 2002).

10. Conclusion

The Siah Kuh unit is a former seamount, now outcropping in the Zagros Suture Zone. It is composed of two units separated by a major thrust, both of which record a comparable magmatic and geodynamic history:

1) The seamount was built around 87 Ma in an intraoceanic forearc/arc setting and witnesses increasing maturity and metasomatism of the mantle wedge through time.

2) A resumption of magmatism occurred around 78–73 Ma in a back-arc-like setting, with a transition from enriched to depleted lavas.

3) The Siah Kuh seamount was later subducted below the Eurasian plate (meanwhile, the B unit was thrust onto the A unit), at ~30 km depth, and thereafter exhumed (Fig. 12a).

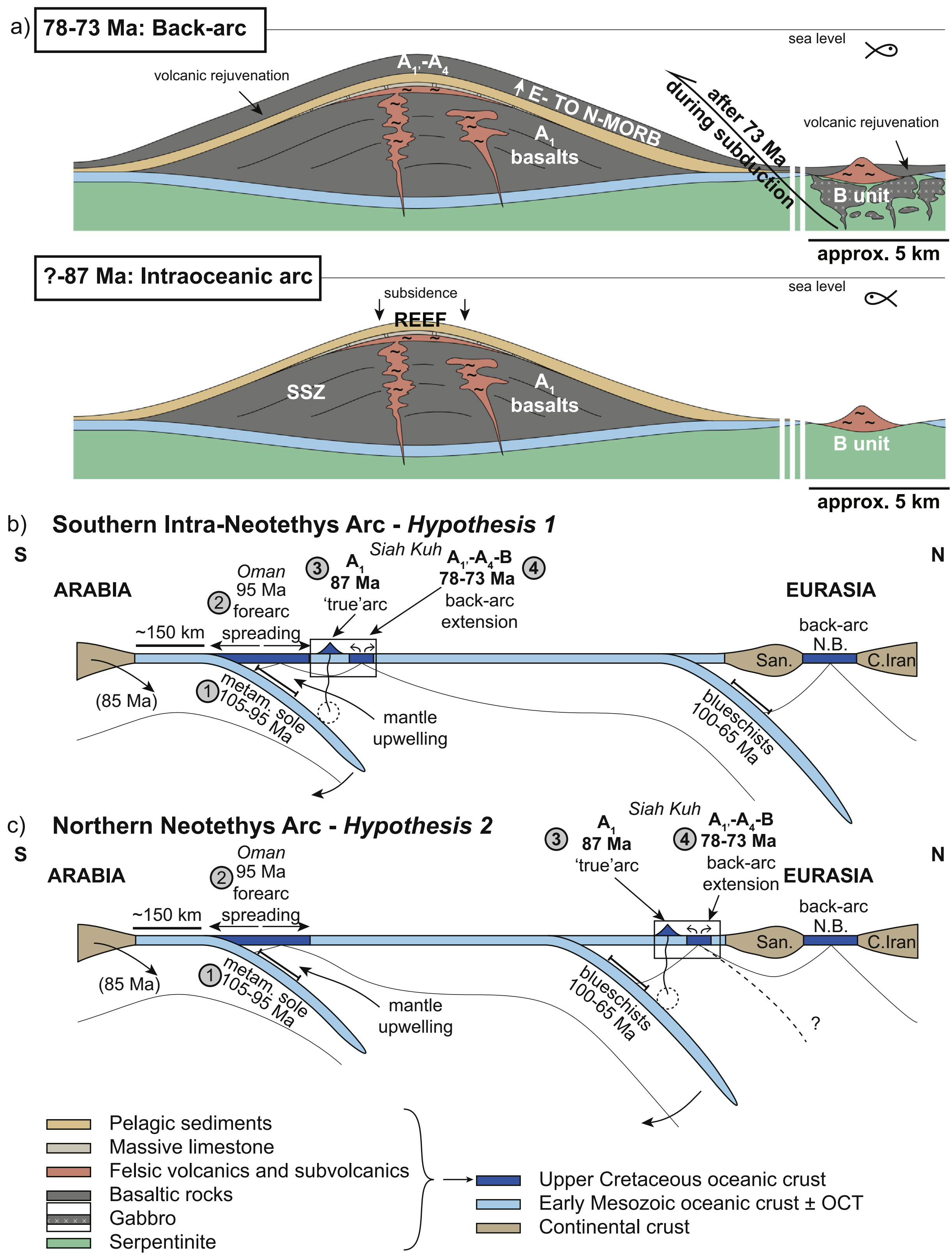

Fig. 12. Synthesis of the tectono-magmatic evolution of the Siah Kuh seamount. a) Two stage evolution of the Siah Kuh seamount during late Cretaceous; b) hypothesis 1: Paleogeographic location of the Siah Kuh seamount as a southern intra-Neotethys arc, c) hypothesis 2: paleogeographic location of the Siah Kuh seamount as an intraoceanic arc in the northern Neotethys. Abbreviations are San. for Sanandaj-Sirjan, N.B. for Nain-Baft, C. Iran for Central Iran.

Combining structural and geochemical data from other magmatic and metamorphic episodes in the Iranian-Omanese Neotethys realm (Table 2), which was affected by two subduction zones during the Late Cretaceous, we propose two possible tectono-magmatic settings for the Siah Kuh seamount. This exceptional remnant might represent (1) an arc located above the Southern Neotethys subduction zone (Fig. 12b), and would therefore represent a non-obducted piece (and the 'missing arc') of the Oman ophiolite, or (2) an arc to forearc domain at the Northern Margin of the Neotethys (Fig. 12c). We consider the first hypothesis more likely (Fig. 12b).

Supplementary data to this article can be found online at https://doi.org/10.1016/j.gr.2019.10.019.

Declaration of competing interest

The authors declare no conflict of interest.

Acknowledgements

This study was partly funded by the project "Zooming in between plates" (Marie Curie International Training Network no. 604713) to P. Agard. We thank M. Fialin and N. Rividi (CAMPARIS) for analytical support, E. Delairis (ISTeP) for the preparation of thin sections, and Hong T. (IGGCAS) and Tan Z. (ISTeP) for help with zircon U-Pb-εHf data collection and processing. M. Rioux, T. John, M. Soret, M. Locatelli and M. Jentzer are thanked for insightful discussions. We thank the anonymous peer-reviewers of this manuscript and A. Festa and M. Santosh for their editorial handling.

References

Agard, P., Monié, P., Gerber, W., Omrani, J., Molinaro, M., Meyer, B., Labrousse, L., Vrielynck, B., Jolivet, L., Yamato, P., 2006. Transient, synobduction exhumation of Zagros blueschists inferred from P-T, deformation, time, and kinematic constraints: implications for Neotethyan wedge dynamics. J. Geophys. Res. 111. https://doi.org/10.1029/2005JB004103 (B11401).

Agard, P., Jolivet, L., Vrielynck, B., Burov, E., Monié, P., 2007. Plate acceleration: the obduction trigger? Earth Planet. Sci. Lett. 258, 428–441. https://doi.org/10.1016/j.epsl.2007.04.002.

Agard, P., Searle, M.P., Alsop, G.I., Dubacq, B., 2010. Crustal stacking and expulsion tectonics during continental subduction: P-T deformation constraints from Oman. Tectonics 29. https://doi.org/10.1029/2010TC002669.

Agard, P., Omrani, J., Jolivet, L., Whitechurch, H., Vrielynck, B., Spakman, W., Monié, P., Meyer, B., Wortel, M.J.R., 2011. Zagros orogeny: a subduction-dominated process. Geol. Mag. 148, 692–725. https://doi.org/10.1017/S001675681100046X.

Agard, P., Zuo, X., Funiciello, F., Bellahsen, N., Faccenna, C., Savva, D., 2014. Obduction: why, how and where. Clues from analog models. Earth Planet. Sci. Lett. 393, 132–145. https://doi.org/10.1016/j.epsl.2014.02.021.

Ahmadipour, H., Sabzehei, M., Whitechurch, H., Rastad, E., Emami, M.H., 2003. Soghan complex as an evidence for paleospreading center and mantle diapirism in Sanandaj-Sirjan Zone (South-East Iran). J. Sci. Islamic Republic Iran 14, 157–172.

Alabaster, T., Pearce, J.A., Malpas, J., 1982. The volcanic stratigraphy and petrogenesis of the Oman ophiolite complex. Contrib. Mineral. Petrol. 81, 168–183. https://doi.org/10.1007/BF00371294.

Ali, S.A., Buckman, S., Aswad, K.J., Jones, B.G., Ismail, S.A., Nutman, A.P., 2012. Recognition of Late Cretaceous Hasanbag ophiolite-arc rocks in the Kurdistan Region of the Iraqi Zagros suture zone: a missing link in the paleogeography of the closing Neotethys Ocean. Lithosphere 4, 395–410. https://doi.org/10.1130/L207.1.

Andersen, T., 2002. Correction of common lead in U-Pb analyses that do not report ^{204}Pb. Chem. Geol. 192, 59–79. https://doi.org/10.1016/S0009-2541(02)00195-X.

Angiboust, S., Agard, P., Glodny, J., Omrani, J., Oncken, O., 2016. Zagros blueschists: episodic underplating and long-lived cooling of a subduction zone. Earth Planet. Sci. Lett. 443, 48–58. https://doi.org/10.1016/j.epsl.2016.03.017.

Ao, S., Xiao, W., Khalatbari Jafari, M., Talebian, M., Chen, L., Wan, B., Ji, W., Zhang, Z., 2016. U–Pb zircon ages, field geology and geochemistry of the Kermanshah ophiolite (Iran): from continental rifting at 79 Ma to oceanic core complex at ca. 36 Ma in the southern Neo-Tethys. Gondwana Res. 31, 305–318. https://doi.org/10.1016/j.gr.2015.01.014.

Arvin, M., Robinson, P.T., 1994. The petrogenesis and tectonic setting of lavas from the Baft Ophiolitic Mélange, southwest of Kerman, Iran. Can. J. Earth Sci. 31, 824–834. https://doi.org/10.1139/e94-076.

Arvin, M., Pan, Y., Dargahi, S., Malekizadeh, A., Babaei, A., 2007. Petrochemistry of the Siah-Kuh granitoid stock southwest of Kerman, Iran: implications for initiation of Neotethys subduction. J. Asian Earth Sci. 30, 474–489. https://doi.org/10.1016/j.jseaes.2007.01.001.

Azizan, H., Naderi, N., Navazi, M., Poshtkuhi, M., Rashid, H., Abazari, Z., Haddadan, M., 2007. Geological Map of Iran, 1:100000 Series - Dolatabad.

Azizi, H., Stern, R.J., 2019. Jurassic igneous rocks of the central Sanandaj–Sirjan zone (Iran) mark a propagating continental rift, not a magmatic arc. Terra Nova 31 (5), 1–9. https://doi.org/10.1111/ter.12404.

Babaie, H.A., Ghazi, A.M., Babaei, A., La Tour, T.E., Hassanipak, A.A., 2001. Geochemistry of arc volcanic rocks of the Zagros Crush Zone, Neyriz, Iran. J. Asian Earth Sci. 19, 61–76. https://doi.org/10.1016/S1367-9120(00)00012-2.

Babaie, H.A., Babaei, A., Ghazi, A.M., Arvin, M., 2006. Geochemical, ^{40}Ar/^{39}Ar age, and isotopic data for crustal rocks of the Neyriz ophiolite, Iran. Can. J. Earth Sci. 43, 57–70. https://doi.org/10.1139/e05-111.

Babazadeh, S.A., de Wever, P., 2004. Early Cretaceous radiolarian assemblages from radiolarites in the Sistan Suture (eastern Iran). Geodiversitas 26, 185–206.

Bagheri, S., Stampfli, G.M., 2008. The Anarak, Jandaq and Posht-e-Badam metamorphic complexes in central Iran: new geological data, relationships and tectonic implications. Tectonophysics 451, 123–155. https://doi.org/10.1016/j.tecto.2007.11.047.

Barbarin, B., 1999. A review of the relationships between granitoid types, their origins and their geodynamic environments. Lithos 46, 605–626. https://doi.org/10.1016/S0024-4937(98)00085-1.

Barnes, S.J., Roeder, P.L., 2001. The range of spinel compositions in terrestrial mafic and ultramafic rocks. J. Petrol. 42, 2279–2302. https://doi.org/10.1093/petrology/42.12.2279.

Barrier, E., Vrielynck, B., 2008. Palaeotectonic maps of the Middle East: Late Maastrichtian. Commission de la Carte Géologique du Monde Map 8.

Batiza, R., Vanko, D., 1984. Petrology of young Pacific Seamounts. J. Geophys. Res. 89, 11,211–235,260. https://doi.org/10.1029/JB089iB13p11235.

Belgrano, T.M., Diamond, L.W., 2019. Subduction-zone contributions to axial volcanism in the Oman–U.A.E. ophiolite. Lithosphere 11, 399–411. https://doi.org/10.1130/L1045.1.

Berberian, F., Berberian, M., 1981. Tectono-plutonic episodes in Iran. In: Gupta, H.K., Delany, F.M. (Eds.), Geodynamics Series, Geodynamics Series. American Geophysical Union, pp. 33–69.

Bonnet, G., Agard, P., Angiboust, S., Monié, P., Jentzer, M., Omrani, J., Whitechurch, H., Fournier, M., 2018. Tectonic slicing and mixing processes along the subduction interface: the Sistan example (Eastern Iran). Lithos 310–311, 269–287. https://doi.org/10.1016/j.lithos.2018.04.016.

Bonnet, G., Agard, P., Angiboust, S., Fournier, M., Omrani, J., 2019a. No large earthquakes in fully exposed subducted seamount. Geology 47, 407–410. https://doi.org/10.1130/G45564.1.

Bonnet, G., Agard, P., Angiboust, S., Monié, P., Fournier, M., Caron, B., Omrani, J., 2019b. Structure and metamorphism of a subducted seamount (Zagros suture, Southern Iran). Geosphere 15. https://doi.org/10.1130/GES02134.1.

Boudier, F., Ceuleneer, G., Nicolas, A., 1988. Shear zones, thrusts and related magmatism in the Oman ophiolite: initiation of thrusting on an oceanic ridge. Tectonophysics 151, 275–296. https://doi.org/10.1016/0040-1951(88)90249-1.

Boutelier, D., Chemenda, A., Burg, J.-P., 2003. Subduction versus accretion of intra-oceanic volcanic arcs: insight from thermo-mechanical analogue experiments. Earth Planet. Sci. Lett. 212, 31–45. https://doi.org/10.1016/S0012-821X(03)00239-5.

Bouvier, A., Vervoort, J.D., Patchett, P.J., 2008. The Lu–Hf and Sm–Nd isotopic composition of CHUR: constraints from unequilibrated chondrites and implications for the bulk composition of terrestrial planets. Earth Planet. Sci. Lett. 273, 48–57. https://doi.org/10.1016/j.epsl.2008.06.010.

Briqueu, L., Bougault, H., Joron, J.L., 1984. Quantification of Nb, Ta, Ti and V anomalies in magmas associated with subduction zones: petrogenetic implications. Earth Planet. Sci. Lett. 68, 297–308.

Briqueu, L., Mével, C., Boudier, F., 1991. Sr, Nd and Pb isotopic constraints in the genesis of a calc-alkaline plutonic suite in Oman ophiolite related to the obduction process. Ophiolite Genesis and Evolution of the Oceanic Lithosphere. Springer, Dordrecht, pp. 517–542.

Burg, J.-P., 2018. Geology of the onshore Makran accretionary wedge: synthesis and tectonic interpretation. Earth Sci. Rev. 185, 1210–1231. https://doi.org/10.1016/j.earscirev.2018.09.011.

Cann, J.R., 1970. Rb, Sr, Y, Zr and Nb in some ocean floor basaltic rocks. Earth Planet. Sci. Lett. 10, 7–11. https://doi.org/10.1016/0012-821X(70)90058-0.

Casey, J.F., Dewey, J.F., 1984. Initiation of subduction zones along transform and accreting plate boundaries, triple-junction evolution, and forearc spreading centres—implications for ophiolitic geology and obduction. Geol. Soc. Lond., Spec. Publ. 13, 269–290. https://doi.org/10.1144/GSL.SP.1984.013.01.22.

Chemenda, A.I., Mattauer, M., Bokun, A.N., 1996. Continental subduction and a mechanism for exhumation of high-pressure metamorphic rocks: new modelling and field data from Oman. Earth Planet. Sci. Lett. 143, 173–182. https://doi.org/10.1016/0012-821X(96)00123-9.

Cloos, M., 1993. Lithospheric buoyancy and collisional orogenesis: subduction of oceanic plateaus, continental margins, island arcs, spreading ridges, and seamounts. Geol. Soc. Am. Bull. 105, 715–737. https://doi.org/10.1130/0016-7606(1993)105<0715:LBACOS>2.3.CO.

Coleman, R.G., 1981. Tectonic setting for ophiolite obduction in Oman. J. Geophys. Res. 86, 2497–2508. https://doi.org/10.1029/JB086iB04p02497.

Davoudian, A.R., Genser, J., Dachs, E., Shabanian, N., 2008. Petrology of eclogites from north of Shahrekord, Sanandaj-Sirjan Zone, Iran. Mineral. Petrol. 92, 393–413. https://doi.org/10.1007/s00710-007-0204-6.

Davoudian, A.R., Genser, J., Neubauer, F., Shabanian, N., 2016. ^{40}Ar/^{39}Ar mineral ages of eclogites from North Shahrekord in the Sanandaj–Sirjan Zone, Iran: implications for the tectonic evolution of Zagros orogen. Gondwana Res. 37, 216–240. https://doi.org/10.1016/j.gr.2016.05.013.

Delaloye, M., Desmons, J., 1980. Ophiolites and melange terranes in Iran: a geochronological study and its paleotectonic implications. Tectonophysics 68, 83–111. https://doi.org/10.1016/0040-1951(80)90009-8.

Delavari, M., Dolati, A., Marroni, M., Pandolfi, L., Saccani, E., 2016. Association of MORB and SSZ ophiolites along the shear zone between coloured Mélange and Bajgan complexes (north Makran, Iran): evidence from the Sorkhband Area. Ofioliti 41 (1), 21–34. https://doi.org/10.4454/ofioliti.v41i1.440.

Dick, H.J.B., Bullen, T., 1984. Chromian spinel as a petrogenetic indicator in abyssal and alpine-type peridotites and spatially associated lavas. Contrib. Mineral. Petrol. 86, 54–76. https://doi.org/10.1007/BF00373711.

Dilek, Y., Furnes, H., Shallo, M., 2008. Geochemistry of the Jurassic Mirdita Ophiolite (Albania) and the MORB to SSZ evolution of a marginal basin oceanic crust. Lithos 100, 174–209. https://doi.org/10.1016/j.lithos.2007.06.026.

Droop, G.T.R., 1987. A general equation for estimating Fe^{3+} concentrations in ferromagnesian silicates and oxides from microprobe analyses, using stoichiometric criteria. Mineral. Mag. 51, 431–435. https://doi.org/10.1180/minmag.1987.051.361.10.

Dupré, B., Allègre, C.J., 1983. Pb–Sr isotope variation in Indian Ocean basalts and mixing phenomena. Nature 303, 142–146. https://doi.org/10.1038/303142a0.

El Shazly, A.E.-D.K., Bröcker, M., Hacker, B.R., Calvert, A.J., 2001. Formation and exhumation of blueschists and eclogites from NE Oman: new perspectives from Rb-Sr and $^{40}Ar/^{39}Ar$ dating. J. Metamorph. Geol. 19, 233–248. https://doi.org/10.1046/j.1525-1314.2001.00309.x.

Faccenna, C., Becker, T.W., Auer, L., Billi, A., Boschi, L., Brun, J.P., Capitanio, F.A., Funiciello, F., Horvàth, F., Jolivet, L., Piromallo, C., Royden, L., Rossetti, F., Serpelloni, E., 2014. Mantle dynamics in the Mediterranean. Rev. Geophys. 52, 283–332. https://doi.org/10.1002/2013RG000444.

Frey, F.A., Weis, D., 1995. Temporal evolution of the Kerguelen plume: geochemical evidence from 38 to 82 Ma lavas forming the Ninetyeast ridge. Contrib. Mineral. Petrol. 121, 12–28. https://doi.org/10.1007/s004100050087.

Gansser, A., 1960. Ausseralpine Ophiolithprobleme. Eclogae Geol. Helv. 52, 659–680.

Gao, J., John, T., Klemd, R., Xiong, X., 2007. Mobilization of Ti–Nb–Ta during subduction: evidence from rutile-bearing dehydration segregations and veins hosted in eclogite, Tianshan, NW China. Geochim. Cosmochim. Acta 71, 4974–4996. https://doi.org/10.1016/j.gca.2007.07.027.

Gharib, F., De Wever, P., 2010. Radiolaires Mésozoïques de la formation de Kermanshah (Iran). CR Palevol 9, 209–219. https://doi.org/10.1016/j.crpv.2010.06.003.

Ghasemi, A., Talbot, C.J., 2006. A new tectonic scenario for the Sanandaj-Sirjan Zone (Iran). J. Asian Earth Sci. 26, 683–693. https://doi.org/10.1016/j.jseaes.2005.01.003.

Ghasemi, H., Juteau, T., Bellon, H., Sabzehei, M., Whitechurch, H., Ricou, L.-E., 2002. The mafic–ultramafic complex of Sikhoran (central Iran): a polygenetic ophiolite complex. Compt. Rendus Geosci. 334, 431–438. https://doi.org/10.1016/S1631-0713(02)01770-4.

Ghazi, A.M., Hassanipak, A.A., Mahoney, J.J., Duncan, R.A., 2004. Geochemical characteristics, ^{40}Ar–^{39}Ar ages and original tectonic setting of the Band-e-Zeyarat/Dar Anar ophiolite, Makran accretionary prism, S.E. Iran. Tectonophysics 393, 175–196. https://doi.org/10.1016/j.tecto.2004.07.035.

Gillis, K.M., 1995. Controls on hydrothermal alteration in a section of fast-spreading oceanic crust. Earth Planet. Sci. Lett. 134, 473–489. https://doi.org/10.1016/0012-821X(95)00137-2.

Gnos, E., Peters, T., 1993. K-Ar ages of the metamorphic sole of the Semail Ophiolite: implications for ophiolite cooling history. Contrib. Mineral. Petrol. 113, 325–332. https://doi.org/10.1007/BF00286925.

Godard, M., Dautria, J.M., Perrin, M., 2003. Geochemical variability of the Oman ophiolite lavas: relationship with spatial distribution and paleomagnetic directions. Geochem. Geophys. Geosyst. 4. https://doi.org/10.1029/2002GC000452.

Godard, M., Bosch, D., Einaudi, F., 2006. A MORB source for low-Ti magmatism in the Semail ophiolite. Chem. Geol. 234, 58–78. https://doi.org/10.1016/j.chemgeo.2006.04.005.

Goodenough, K.M., Styles, M.T., Schofield, D., Thomas, R.J., Crowley, Q.C., Lilly, R.M., McKervey, J., Stephenson, D., Carney, J.N., 2010. Architecture of the Oman–UAE ophiolite: evidence for a multi-phase magmatic history. Arab. J. Geosci. 3, 439–458. https://doi.org/10.1007/s12517-010-0177-3.

Guilmette, C., Smit, M.A., van Hinsbergen, D.J.J., Gürer, D., Corfu, F., Charette, B., Maffione, M., Rabeau, O., Savard, D., 2018. Forced subduction initiation recorded in the sole and crust of the Semail Ophiolite of Oman. Nat. Geosci. 11, 688–695. https://doi.org/10.1038/s41561-018-0209-2.

Haase, K.M., Freund, S., Koepke, J., Hauff, F., Erdmann, M., 2015. Melts of sediments in the mantle wedge of the Oman ophiolite. Geology 43, 275–278. https://doi.org/10.1130/G36451.1.

Hacker, B.R., Mosenfelder, J.L., Gnos, E., 1996. Rapid emplacement of the Oman ophiolite: thermal and geochronologic constraints. Tectonics 15, 1230–1247. https://doi.org/10.1029/96TC01973.

Hassanzadeh, J., Wernicke, B.P., 2016. The Neotethyan Sanandaj-Sirjan zone of Iran as an archetype for passive margin-arc transitions. Tectonics 35, 586–621. https://doi.org/10.1002/2015TC003926.

Hastie, A.R., Kerr, A.C., Pearce, J.A., Mitchell, S.F., 2007. Classification of altered volcanic island arc rocks using immobile trace elements: development of the Th–Co discrimination diagram. J. Petrol. 48, 2341–2357. https://doi.org/10.1093/petrology/egm062.

Hauff, F., Hoernle, K., Schmincke, H.-U., Werner, R., 1997. A Mid Cretaceous origin for the Galápagos hotspot: volcanological, petrological and geochemical evidence from Costa Rican oceanic crustal segments. Geol. Rundsch. 86, 141–155. https://doi.org/10.1007/PL00009938.

Hauff, F., Hoernle, K., Schmidt, A., 2003. Sr-Nd-Pb composition of Mesozoic Pacific oceanic crust (Site 1149 and 801, ODP Leg 185): implications for alteration of ocean crust and the input into the Izu-Bonin-Mariana subduction system: SR-ND-PB COMPOSITION OF MESOZOIC PACIFIC. Geochem. Geophys. Geosyst. 4. https://doi.org/10.1029/2002GC000421.

Hawkins, J.W., Bloomer, S.H., Evans, C.A., Melchior, J.T., 1984. Evolution of intra-oceanic arc-trench systems. Tectonophysics 102, 175–205. https://doi.org/10.1016/0040-1951(84)90013-1.

Hémond, C., Hofmann, A.W., Vlastélic, I., Nauret, F., 2006. Origin of MORB enrichment and relative trace element compatibilities along the Mid-Atlantic Ridge between 10° and 24°N. Geochem. Geophys. Geosyst. 7. https://doi.org/10.1029/2006GC001317.

Hochstaedter, A., Gill, J., Peters, R., Broughton, P., Holden, P., Taylor, B., 2001. Across-arc geochemical trends in the Izu-Bonin arc: contributions from the subducting slab. Geochem. Geophys. Geosyst. 2. https://doi.org/10.1029/2000GC000105.

Hu, Z., Liu, Y., Gao, S., Xiao, S., Zhao, L., Günther, D., Li, M., Zhang, W., Zong, K., 2012. A "wire" signal smoothing device for laser ablation inductively coupled plasma mass spectrometry analysis. Spectrochim. Acta B At. Spectrosc. 78, 50–57. https://doi.org/10.1016/j.sab.2012.09.007.

Humphris, S.E., Thompson, G., 1978. Trace element mobility during hydrothermal alteration of oceanic basalts. Geochim. Cosmochim. Acta 42, 127–136. https://doi.org/10.1016/0016-7037(78)90222-3.

Hunziker, D., Burg, J.-P., Bouilhol, P., von Quadt, A., 2015. Jurassic rifting at the Eurasian Tethys margin: geochemical and geochronological constraints from granitoids of North Makran, southeastern Iran. Tectonics 34, 571–593. https://doi.org/10.1002/2014TC003768.

Hunziker, D., Burg, J.-P., Moulas, E., Reusser, E., Omrani, J., 2017. Formation and preservation of fresh lawsonite: geothermobarometry of the North Makran Blueschists, southeast Iran. J. Metamorph. Geol. 35, 871–895. https://doi.org/10.1111/jmg.12259.

Ishikawa, T., Nagaishi, K., Umino, S., 2002. Boninitic volcanism in the Oman ophiolite: Implications for thermal condition during transition from spreading ridge to arc. Geology 30, 899–902. https://doi.org/10.1130/0091-7613(2002)030<0899:BVITOO>2.0.CO;2.

Ishikawa, T., Fujisawa, S., Nagaishi, K., Masuda, T., 2005. Trace element characteristics of the fluid liberated from amphibolite-facies slab: inference from the metamorphic sole beneath the Oman ophiolite and implication for boninite genesis. Earth Planet. Sci. Lett. 240, 355–377. https://doi.org/10.1016/j.epsl.2005.09.049.

Ishizuka, O., Tani, K., Reagan, M.K., Kanayama, K., Umino, S., Harigane, Y., Sakamoto, I., Miyajima, Y., Yuasa, M., Dunkley, D.J., 2011. The timescales of subduction initiation and subsequent evolution of an oceanic island arc. Earth Planet. Sci. Lett. 306, 229–240. https://doi.org/10.1016/j.epsl.2011.04.006.

Jafari, A., Fazlnia, A., Jamei, S., 2018. Geochemistry, petrology and geodynamic setting of the Urumieh plutonic complex, Sanandaj–Sirjan zone, NW Iran: new implication for Arabian and Central Iranian plate collision. J. Afr. Earth Sci. 139, 421–439. https://doi.org/10.1016/j.jafrearsci.2017.11.039.

Jannessary, M.R., 2003. Les ophiolites de Neyriz (Sud de l'Iran): Naissance d'une dorsale en pied de marge continentale (étude des structures internes, de la fabrique du manteau, et de l'évolution pétro-géochimique des magmas). (PhD thesis). Université Louis Pasteur, Strasbourg.

Jannessary, M.R., Whitechurch, H., 2008. The birth of an oceanic crust at the foot of Gondwana margin (Neyriz ophiolite, Iran). Geosciences 17, 41–48.

John, T., Scherer, E.E., Schenk, V., Herms, P., Halama, R., Garbe-Schönberg, C.-D., 2010. Subducted seamounts in an eclogite-facies ophiolite sequence: the Andean Raspas Complex, SW Ecuador. Contrib. Mineral. Petrol. 159, 265–284. https://doi.org/10.1007/s00410-009-0427-0.

Kananian, A., Juteau, T., Bellon, H., Darvishzadeh, A., Sabzehi, M., Whitechurch, H., Ricou, L.-E., 2001. The ophiolite massif of Kahnuj (western Makran, southern Iran): new geological and geochronological data. C. R. Acad. Sci. Ser. IIA Earth Planet. Sci. 332, 543–552. https://doi.org/10.1016/S1251-8050(01)01574-9.

Kawahata, H., Nohara, M., Ishizuka, H., Hasebe, S., Chiba, H., 2001. Sr isotope geochemistry and hydrothermal alteration of the Oman ophiolite. J. Geophys. Res. 106, 11083–11099. https://doi.org/10.1029/2000JB900456.

Kazemi, Z., Ghasemi, H., Tilhac, R., Griffin, W., Moghadam, H.S., O'Reilly, S., Mousivand, F., 2019. Journal of the Geological Society 176 (3), 530–552. https://doi.org/10.1144/jgs2018-076.

Khalatbari-Jafari, M., Juteau, T., Bellon, H., Whitechurch, H., Cotten, J., Emami, H., 2004. New geological, geochronological and geochemical investigations on the Khoy ophiolites and related formations, NW Iran. J. Asian Earth Sci. 23, 507–535. https://doi.org/10.1016/j.jseaes.2003.07.005.

König, S., Münker, C., Schuth, S., Luguet, A., Hoffmann, J.E., Kuduon, J., 2010. Boninites as windows into trace element mobility in subduction zones. Geochim. Cosmochim. Acta 74, 684–704. https://doi.org/10.1016/j.gca.2009.10.011.

Kusano, Y., Hayashi, M., Adachi, Y., Umino, S., Miyashita, S., 2014. Evolution of volcanism and magmatism during initial arc stage: constraints on the tectonic setting of the Oman Ophiolite. Geol. Soc. Lond., Spec. Publ. 392, 177–193. https://doi.org/10.1144/SP392.9.

Kusano, Y., Umino, S., Shinjo, R., Ikei, A., Adachi, Y., Miyashita, S., Arai, S., 2017. Contribution of slab-derived fluid and sedimentary melt in the incipient arc magmas with development of the paleo-arc in the Oman Ophiolite. Chem. Geol. 449, 206–225. https://doi.org/10.1016/j.chemgeo.2016.12.012.

Lachize, M., Lorand, J.P., Juteau, T., 1996. Calc-alkaline differentiation trend in the plutonic sequence of the Wadi Haymiliyah section, Haylayn massif, Semail ophiolite, Oman. Lithos 38, 207–232. https://doi.org/10.1016/0024-4937(96)00009-6.

Lanphere, M.A., Pamić, J., 1983. Ages and tectonic setting of ophiolite from the Neyriz area, southeast Zagros Range, Iran. Tectonophysics 96, 245–256. https://doi.org/10.1016/0040-1951(83)90220-2.

Lapierre, H., 2004. The Tethyan plume: geochemical diversity of Middle Permian basalts from the Oman rifted margin. Lithos 74, 167–198. https://doi.org/10.1016/j.lithos.2004.02.006.

Leterrier, J., Maury, R.C., Thonon, P., Girard, D., Marchal, M., 1982. Clinopyroxene composition as a method of identification of the magmatic affinities of paleo-volcanic series. Science 59, 139–154.

Lippard, S.J., Shelton, A.W., Gass, I.G., 1986. The Ophiolite of Northern Oman (The Geological Society. ed).
Liu, Y., Hu, Z., Gao, S., Günther, D., Xu, J., Gao, C., Chen, H., 2008. In situ analysis of major and trace elements of anhydrous minerals by LA-ICP-MS without applying an internal standard. Chem. Geol. 257, 34–43. https://doi.org/10.1016/j.chemgeo.2008.08.004.
Liu, Y., Gao, S., Hu, Z., Gao, C., Zong, K., Wang, D., 2010. Continental and oceanic crust recycling-induced melt-peridotite interactions in the trans-North China Orogen: U-Pb dating, Hf isotopes and trace elements in zircons from mantle xenoliths. J. Petrol. 51, 537–571. https://doi.org/10.1093/petrology/egp082.
Ludwig, K.R., 2001. Users Manual for Isoplot/Ex.: A Geochronological Toolkit for Microsoft Excel.
MacPherson, G.T., 1983. The Snow Mountain Volcanic Complex: an on-land seamount in the Franciscan Terrain, California. J. Geol. 91, 73–92.
Madjidi, B., Berberian, M., Hushmandzadeh, A., Nowgole-Sadat, M.A.A., Sabzehei, M., Alavi-Tehrani, N., Azizan, H., Nazemzadeh, M., Roshan ravan-H, J., Afaghe, A., Afsharianzadeh, A.M., Dehhaghe, F., Ghomashi, A., 1993. Geological Map of Iran, 1: 250000 Series - Haji Abad.
Malavieille, J., Lallemand, S.E., Dominguez, S., Deschamps, A., Lu, C.-Y., Liu, C.-S., Schnuerle, P., Angelier, J., Collot, J.Y., Deffontaines, B., Fournier, M., Hsu, S.K., Le Formal, J.P., Liu, S.Y., Sibuet, J.C., Thareau, N., Wang, F., the ACT (Active Collision in Taiwan) Scientific Crew, 2002. Arc-continent collision in Taiwan: new marine observations and tectonic evolution. Special Paper 358: Geology and Geophysics of an Arc-continent Collision, Taiwan. Geological Society of America , pp. 187–211. https://doi.org/10.1130/0-8137-2358-2.187.
Martin, H., 1999. Adakitic magmas: modern analogues of Archaean granitoids. Lithos 46, 411–429. https://doi.org/10.1016/S0024-4937(98)00076-0.
Mazhari, S.A., Klötzli, U., Safari, M., 2019. Petrological investigation of Late Cretaceous magmatism in Kaboodan area, NE Iran: evidence for an active continental arc at Sabzevar zone. Lithos 348–349, 1–18. https://doi.org/10.1016/j.lithos.2019.105183.
McCall, G.J.H., 1997. The geotectonic history of the Makran and adjacent areas of southern Iran. J. Asian Earth Sci. 15, 517–531. https://doi.org/10.1016/S0743-9547(97)00032-9.
McCulloch, M.T., Gregory, R.T., Wasserburg, G.J., Taylor, H.P., 1981. Sm-Nd, Rb-Sr, and $^{18}O/^{16}O$ isotopic systematics in an oceanic crustal section: evidence from the Samail Ophiolite. J. Geophys. Res. Solid Earth 86, 2721–2735. https://doi.org/10.1029/JB086iB04p02721.
Michael, P., 1995. Regionally distinctive sources of depleted MORB: evidence from trace elements and H_2O. Earth Planet. Sci. Lett. 131, 301–320. https://doi.org/10.1016/0012-821X(95)00023-6.
Moghadam, H.S., Stern, R.J., 2015. Ophiolites of Iran: keys to understanding the tectonic evolution of SW Asia: (II) Mesozoic ophiolites. J. Asian Earth Sci. 100, 31–59. https://doi.org/10.1016/j.jseaes.2014.12.016.
Moghadam, H.S., Whitechurch, H., Rahgoshay, M., Monsef, I., 2009. Significance of Nain-Baft ophiolitic belt (Iran): short-lived, transtensional Cretaceous back-arc oceanic basins over the Tethyan subduction zone. Compt. Rendus Geosci. 341, 1016–1028. https://doi.org/10.1016/j.crte.2009.06.011.
Moghadam, H.S., Stern, R.J., Rahgoshay, M., 2010. The Dehshir ophiolite (central Iran): geochemical constraints on the origin and evolution of the Inner Zagros ophiolite belt. Geol. Soc. Am. Bull. 122, 1516–1547. https://doi.org/10.1130/B30066.1.
Moghadam, H.S., Corfu, F., Stern, R.J., 2013a. U–Pb zircon ages of late cretaceous Nain Dehshir ophiolites, central Iran. J. Geol. Soc. Lond. 170, 175–184. https://doi.org/10.1144/jgs2012-066.U.
Moghadam, H.S., Mosaddegh, H., Santosh, M., 2013b. Geochemistry and petrogenesis of the Late Cretaceous Haji-Abad ophiolite (Outer Zagros Ophiolite Belt, Iran): implications for geodynamics of the Bitlis-Zagros suture zone. Geol. J. 48, 579–602. https://doi.org/10.1002/gj.2458.
Moghadam, H.S., Stern, R.J., Chiaradia, M., Rahgoshay, M., 2013c. Geochemistry and tectonic evolution of the Late Cretaceous Gogher–Baft ophiolite, central Iran. Lithos 168–169, 33–47. https://doi.org/10.1016/j.lithos.2013.01.013.
Moghadam, H.S., Corfu, F., Chiaradia, M., Stern, R.J., Ghorbani, G., 2014a. Sabzevar Ophiolite, NE Iran: progress from embryonic oceanic lithosphere into magmatic arc constrained by new isotopic and geochemical data. Lithos 210–211, 224–241. https://doi.org/10.1016/j.lithos.2014.10.004.
Moghadam, H.S., Zaki Khedr, M., Chiaradia, M., Stern, R.J., Bakhshizad, F., Arai, S., Ottley, C.J., Tamura, A., 2014b. Supra-subduction zone magmatism of the Neyriz ophiolite, Iran: constraints from geochemistry and Sr-Nd-Pb isotopes. Int. Geol. Rev. 56, 1395–1412. https://doi.org/10.1080/00206814.2014.942391.
Moghadam, H.S., Bröcker, M., Griffin, W.L., Li, X.H., Chen, R.-X., O'Reilly, S.Y., 2017. Subduction, high-P metamorphism, and collision fingerprints in South Iran: constraints from zircon U-Pb and mica Rb-Sr geochronology. Geochem. Geophys. Geosyst. 18, 306–332. https://doi.org/10.1002/2016GC006585.
Mohammadi, A., Burg, J.-P., Guillong, M., von Quadt, A., 2017. Arc magmatism witnessed by detrital zircon U-Pb geochronology, Hf isotopes and provenance analysis of Late Cretaceous-Miocene sandstones of onshore western Makran (SE Iran). Am. J. Sci. 317, 941–964. https://doi.org/10.2475/08.2017.03.
Moll, M., Paulick, H., Suhr, G., Bach, W., 2007. Data report: microprobe analyses of primary phases (olivine, pyroxene, and spinel) and alteration products (serpentine, iowaite, talc, magnetite, and sulfides) in Holes 1268A, 1272A, and 1274A. Proceedings of the Ocean Drilling Program, Scientific Results. Ocean Drilling Program College Station, TX, pp. 1–13.
Monié, P., Agard, P., 2009. Coeval blueschist exhumation along thousands of kilometers: implications for subduction channel processes. Geochem. Geophys. Geosyst. 10. https://doi.org/10.1029/2009GC002428.
Monsef, I., Monsef, R., Mata, J., Zhang, Z., Pirouz, M., Rezaeian, M., Esmaeili, R., Xiao, W., 2018a. Evidence for an early-MORB to fore-arc evolution within the Zagros suture zone: constraints from zircon U-Pb geochronology and geochemistry of the Neyriz ophiolite (South Iran). Gondwana Res. 62, 287–305. https://doi.org/10.1016/j.gr.2018.03.002.
Monsef, I., Rahgoshay, M., Pirouz, M., Chiaradia, M., Grégoire, M., Ceuleneer, G., 2018b. The Eastern Makran Ophiolite (SE Iran): evidence for a Late Cretaceous fore-arc oceanic crust. Int. Geol. Rev., 1–27 https://doi.org/10.1080/00206814.2018.1507764.
Morris, A., Meyer, M., Anderson, M.W., MacLeod, C.J., 2016. Clockwise rotation of the entire Oman ophiolite occurred in a suprasubduction zone setting. Geology 44, 1055–1058. https://doi.org/10.1130/G38380.1.
Nazemzadeh, M., Rashidi, A., Navazi, M., Poshtkuhi, M., Davari, M., Ezatian, F., Sabzehei, M., Atapour, H., Haddadan, M., 2007. Geological Map of Iran, 1:100000 Series - Dehsard (Bazar).
Niu, Y., Collerson, K.D., Batiza, R., Wendt, J.I., Regelous, M., 1999. Origin of enriched-type mid-ocean ridge basalt at ridges far from mantle plumes: the East Pacific Rise at 11°20′N. J. Geophys. Res. Solid Earth 104, 7067–7087. https://doi.org/10.1029/1998JB900037.
Omrani, J., Agard, P., Whitechurch, H., Benoit, M., Prouteau, G., Jolivet, L., 2008. Arc-magmatism and subduction history beneath the Zagros Mountains, Iran: a new report of adakites and geodynamic consequences. Lithos 106, 380–398. https://doi.org/10.1016/j.lithos.2008.09.008.
Park, J.-O., Tsuru, T., Kodaira, S., Cummins, P.R., Kaneda, Y., 2002. Splay fault branching along the Nankai subduction zone. Science 297, 1157–1160. https://doi.org/10.1126/science.1074111.
Patchett, P.J., 1983. Importance of the Lu-Hf isotopic system in studies of planetary chronology and chemical evolution. Geochim. Cosmochim. Acta 47, 81–91. https://doi.org/10.1016/0016-7037(83)90092-3.
Pearce, J.A., 1996. A Users Guide to Basalt Discrimination Diagrams. Geological Association of Canada, Short Course Notes.
Pearce, J.A., 2008. Geochemical fingerprinting of oceanic basalts with applications to ophiolite classification and the search for Archean oceanic crust. Lithos 100, 14–48. https://doi.org/10.1016/j.lithos.2007.06.016.
Pearce, J.A., Lippard, S.J., Roberts, S., 1984. Characteristics and tectonic significance of supra-subduction zone ophiolites. Geol. Soc. Lond., Spec. Publ. 16, 77–94. https://doi.org/10.1144/GSL.SP.1984.016.01.06.
Pearce, J.A., Stern, R.J., Bloomer, S.H., Fryer, P., 2005. Geochemical mapping of the Mariana arc-basin system: implications for the nature and distribution of subduction components. Geochem. Geophys. Geosyst. 6. https://doi.org/10.1029/2004GC000895.
Péron-Pinvidic, G., Manatschal, G., 2009. The final rifting evolution at deep magma-poor passive margins from Iberia-Newfoundland: a new point of view. Int. J. Earth Sci. 98, 1581–1597. https://doi.org/10.1007/s00531-008-0337-9.
Pirnia, T., Saccani, E., Torabi, G., Chiari, M., Goričan, Š., Barbero, E., 2019. Cretaceous tectonic evolution of the Neo-Tethys in Central Iran: evidence from petrology and age of the Nain-Ashin ophiolitic basalts. Geosci. Front. S1674987119300647. https://doi.org/10.1016/j.gsf.2019.02.008.
Plank, T., 2005. Constraints from thorium/lanthanum on sediment recycling at subduction zones and the evolution of the continents. J. Petrol. 46, 921–944. https://doi.org/10.1093/petrology/egi005.
Plank, T., Langmuir, C.H., 1998. The chemical composition of subducting sediment and its consequences for the crust and mantle. Chem. Geol. 145, 325–394. https://doi.org/10.1016/S0009-2541(97)00150-2.
Ranero, C.R., von Huene, R., 2000. Subduction erosion along the Middle America convergent margin. Nature 404, 748–752. https://doi.org/10.1038/35008046.
Ricou, L.-E., 1974. L'étude géologique de la région de Neyriz (Zagros iranien) et l'évolution structurale des Zagrides. (PhD thesis). Université d'Orsay.
Ricou, L.-E., Braud, J., Brunn, J.H., 1977. Le Zagros. Livre à La Mémoire de A.F. de Lapparent (1905–1975), Mémoire Hors-Série de La Société Géologique de France.
Rioux, M., Bowring, S., Kelemen, P., Gordon, S., Dudás, F., Miller, R., 2012. Rapid crustal accretion and magma assimilation in the Oman-U.A.E. ophiolite: high precision U-Pb zircon geochronology of the gabbroic crust. J. Geophys. Res. Solid Earth 117. https://doi.org/10.1029/2012JB009273.
Rioux, M., Bowring, S., Kelemen, P., Gordon, S., Miller, R., Dudás, F., 2013. Tectonic development of the Samail ophiolite: high-precision U-Pb zircon geochronology and Sm-Nd isotopic constraints on crustal growth and emplacement. J. Geophys. Res. Solid Earth 118, 2085–2101. https://doi.org/10.1002/jgrb.50139.
Rioux, M., Garber, J., Bauer, A., Bowring, S., Searle, M., Kelemen, P., Hacker, B., 2016. Synchronous formation of the metamorphic sole and igneous crust of the Semail ophiolite: new constraints on the tectonic evolution during ophiolite formation from high-precision U–Pb zircon geochronology. Earth Planet. Sci. Lett. 451, 185–195. https://doi.org/10.1016/j.epsl.2016.06.051.
Rollinson, H., 2015. Slab and sediment melting during subduction initiation: granitoid dykes from the mantle section of the Oman ophiolite. Contrib. Mineral. Petrol. 170. https://doi.org/10.1007/s00410-015-1177-9.
Rossetti, F., Nasrabady, M., Vignaroli, G., Theye, T., Gerdes, A., Razavi, M.H., Vaziri, H.M., 2010. Early Cretaceous migmatitic mafic granulites from the Sabzevar range (NE Iran): implications for the closure of the Mesozoic peri-Tethyan oceans in central Iran. Terra Nova 22, 26–34. https://doi.org/10.1111/j.1365-3121.2009.00912.x.
Rossetti, F., Nasrabady, M., Theye, T., Gerdes, A., Monié, P., Lucci, F., Vignaroli, G., 2014. Adakite differentiation and emplacement in a subduction channel: the late Paleocene Sabzevar magmatism (NE Iran). Geol. Soc. Am. Bull. 126, 317–343. https://doi.org/10.1130/B30913.1.
Sabzehei, M., 1974. Les mélanges ophiolitiques de la région d'Esfandagheh (Iran méridional) - Etude pétrologique et structurale - Interprétation dans le cadre iranien. Université Scientifique et Médicale de Grenoble.
Saccani, E., Allahyari, K., Beccaluva, L., Bianchini, G., 2013. Geochemistry and petrology of the Kermanshah ophiolites (Iran): implication for the interaction between passive rifting, oceanic accretion, and OIB-type components in the Southern Neo-Tethys Ocean. Gondwana Res. 24, 392–411. https://doi.org/10.1016/j.gr.2012.10.009.

Saccani, E., Delavari, M., Dolati, A., Marroni, M., Pandolfi, L., Chiari, M., Barbero, E., 2018. New insights into the geodynamics of Neo-Tethys in the Makran area: evidence from age and petrology of ophiolites from the Coloured Mélange Complex (SE Iran). Gondwana Res. 62, 306–327. https://doi.org/10.1016/j.gr.2017.07.013.

Schnur, S.R., Gilbert, L.A., 2012. Detailed volcanostratigraphy of an accreted seamount: implications for intraplate seamount formation. Geochem. Geophys. Geosyst. 13, 1–13. https://doi.org/10.1029/2012GC004301.

Searle, M.P., 1980. The Metamorphic Sheet and Underlying Volcanic Rocks beneath the Semail Ophiolite in the Northern Oman Mountains of Arabia.

Searle, M., Cox, J., 1999. Tectonic setting, origin, and obduction of the Oman ophiolite. Geol. Soc. Am. Bull. 111, 104–122.

Searle, M.P., Graham, G.M., 1982. "Oman Exotics"—oceanic carbonate build-ups associated with the early stages of continental rifting. Geology 10, 43. https://doi.org/10.1130/0091-7613(1982)10<43:OECBAW>2.0.CO;2.

Searle, M.P., Warren, C.J., Waters, D.J., Parrish, R.R., 2004. Structural evolution, metamorphism and restoration of the Arabian continental margin, Saih Hatat region, Oman Mountains. J. Struct. Geol. 26, 451–473. https://doi.org/10.1016/j.jsg.2003.08.005.

Seifert, K., Gibson, I., Weis, D., Brunotte, D., 1996. Geochemistry of metamorphosed cumulate gabbros from Hole 900A, Iberia Abyssal Plain. In: Whitmarsh, R.B., Sawyer, D.S., Klaus, A., Masson, D.G. (Eds.), Proceedings of the Ocean Drilling Program, 149 Scientific Results, Proceedings of the Ocean Drilling Program. Ocean Drilling Program. https://doi.org/10.2973/odp.proc.sr.149.1996.

Shahbazi, H., Siebel, W., Pourmoafee, M., Ghorbani, M., Sepahi, A.A., Shang, C.K., Vousoughi Abedini, M., 2010. Geochemistry and U–Pb zircon geochronology of the Alvand plutonic complex in Sanandaj–Sirjan Zone (Iran): new evidence for Jurassic magmatism. J. Asian Earth Sci. 39, 668–683. https://doi.org/10.1016/j.jseaes.2010.04.014.

Shervais, J.W., 1982. TiV plots and the petrogenesis of modern and ophiolitic lavas. Earth Planet. Sci. Lett. 59, 101–118. https://doi.org/10.1016/0012-821X(82)90120-0.

Sláma, J., Košler, J., Condon, D.J., Crowley, J.L., Gerdes, A., Hanchar, J.M., Horstwood, M.S.A., Morris, G.A., Nasdala, L., Norberg, N., Schaltegger, U., Schoene, B., Tubrett, M.N., Whitehouse, M.J., 2008. Plešovice zircon — a new natural reference material for U–Pb and Hf isotopic microanalysis. Chem. Geol. 249, 1–35. https://doi.org/10.1016/j.chemgeo.2007.11.005.

Söderlund, U., Patchett, P.J., Vervoort, J.D., Isachsen, C.E., 2004. The ^{176}Lu decay constant determined by Lu–Hf and U–Pb isotope systematics of Precambrian mafic intrusions. Earth Planet. Sci. Lett. 219, 311–324. https://doi.org/10.1016/S0012-821X(04)00012-3.

Soret, M., Agard, P., Dubacq, B., Plunder, A., Yamato, P., 2017. Petrological evidence for stepwise accretion of metamorphic soles during subduction infancy (Semail ophiolite, Oman and UAE). J. Metamorph. Geol. 35, 1051–1080. https://doi.org/10.1111/jmg.12267.

Spilde, M.N., Brearley, A.J., Papike, J.J., 1993. Alteration of plagioclase and pyroxene phenocrysts in a fissure fumarole, Valley of Ten Thousand Smokes, Alaska. Am. Mineral. 78, 1066–1081.

Staudigel, H., Koppers, A., Lavelle, J.W., Pitcher, T.J., Shank, T.M., 2010. Box 1: defining the word "seamount". Oceanography 23, 20–21.

Stern, R.J., Bloomer, S.H., 1992. Subduction zone infancy: examples from the Eocene Izu-Bonin-Mariana and Jurassic California arcs. Geol. Soc. Am. Bull. 104, 1621–1636. https://doi.org/10.1007/s13398-014-0173-7.2.

Stern, R.J., Lin, P.-N., Morris, J.D., Jackson, M.C., Fryer, P., Bloomer, S.H., Ito, E., 1990. Enriched back-arc basin basalts from the northern Mariana Trough: implications for the magmatic evolution of back-arc basins. Earth Planet. Sci. Lett. 100, 210–225. https://doi.org/10.1016/0012-821X(90)90186-2.

Stöcklin, J., 1981. A brief report on the geodynamics of Iran. Zagros Hindu Kush Himalaya Geodynamic Evolution, pp. 70–74.

Sun, S.-S., McDonough, W.F., 1989. Chemical and isotopic systematics of oceanic basalts: implications for mantle composition and processes. Geol. Soc. Lond., Spec. Publ. 42, 313–345. https://doi.org/10.1144/GSL.SP.1989.042.01.19.

Tiezzi, L.J., Scott, R.B., 1980. Crystal fractionation in a Cumulate Gabbro, Mid-Atlantic Ridge, 26°N. J. Geophys. Res. 85, 5438. https://doi.org/10.1029/JB085iB10p05438.

Tirrul, R., Bell, I.R., Griffis, R.J., Camp, V.E., 1983. The Sistan suture zone of eastern Iran. Geol. Soc. Am. Bull. 94, 134–150. https://doi.org/10.1130/0016-7606(1983)94<134.

Umino, S., 2012. Emplacement mechanism of off-axis large submarine lava field from the Oman Ophiolite. J. Geophys. Res. Solid Earth 117. https://doi.org/10.1029/2012JB009198.

van der Meer, D.G., van Hinsbergen, D.J.J., Spakman, W., 2018. Atlas of the underworld: slab remnants in the mantle, their sinking history, and a new outlook on lower mantle viscosity. Tectonophysics 723, 309–448. https://doi.org/10.1016/j.tecto.2017.10.004.

van Hinsbergen, D.J.J., Maffione, M., Koornneef, L.M.T., Guilmette, C., 2019. Kinematic and paleomagnetic restoration of the Semail ophiolite (Oman) reveals subduction initiation along an ancient Neotethyan fracture zone. Earth Planet. Sci. Lett. 518, 183–196. https://doi.org/10.1016/j.epsl.2019.04.038.

Vervoort, J.D., Blichert-Toft, J., 1999. Evolution of the depleted mantle: Hf isotope evidence from juvenile rocks through time. Geochim. Cosmochim. Acta 63, 533–556. https://doi.org/10.1016/S0016-7037(98)00274-9.

Volpe, A.M., Douglas Macdougall, J., Hawkins, J.W., 1988. Lau Basin basalts (LBB): trace element and Sr-Nd isotopic evidence for heterogeneity in backarc basin mantle. Earth Planet. Sci. Lett. 90, 174–186. https://doi.org/10.1016/0012-821X(88)90099-4.

Warren, C.J., Waters, D.J., 2006. Oxidized eclogites and garnet-blueschists from Oman: P-T path modelling in the NCFMASHO system. J. Metamorph. Geol. 24, 783–802. https://doi.org/10.1111/j.1525-1314.2006.00668.x.

Warren, C.J., Parrish, R.R., Waters, D.J., Searle, M.P., 2005. Dating the geologic history of Oman's Semail ophiolite: insights from U-Pb geochronology. Contrib. Mineral. Petrol. 150, 403–422. https://doi.org/10.1007/s00410-005-0028-5.

Whitechurch, H., Omrani, J., Agard, P., Humbert, F., Montigny, R., Jolivet, L., 2013. Evidence for Paleocene-Eocene evolution of the foot of the Eurasian margin (Kermanshah ophiolite, SW Iran) from back-arc to arc: implications for regional geodynamics and obduction. Lithos 182–183, 11–32. https://doi.org/10.1016/j.lithos.2013.07.017.

Wood, D.A., 1980. The Application of a Th-Hf-Ta diagrams to problems of tectonomagmatic classification and to establish the nature of crustal contaminants of basaltic lavas of the British Tertiary volcanic province. Earth Planet. Sci. Lett. 50, 11–30.

Wrobel-Daveau, J.-C., Ringenbach, J.-C., Tavakoli, S., Ruiz, G.M.H., Masse, P., Frizon de Lamotte, D., 2010. Evidence for mantle exhumation along the Arabian margin in the Zagros (Kermanshah area, Iran). Arab. J. Geosci. 3, 499–513. https://doi.org/10.1007/s12517-010-0209-z.

Wu, F.-Y., Yang, Y.-H., Xie, L.-W., Yang, J.-H., Xu, P., 2006. Hf isotopic compositions of the standard zircons and baddeleyites used in U–Pb geochronology. Chem. Geol. 234, 105–126. https://doi.org/10.1016/j.chemgeo.2006.05.003.

Xu, J.-F., Castillo, P.R., 2004. Geochemical and Nd–Pb isotopic characteristics of the Tethyan asthenosphere: implications for the origin of the Indian Ocean mantle domain. Tectonophysics 393, 9–27. https://doi.org/10.1016/j.tecto.2004.07.028.

Yamato, P., Agard, P., Goffé, B., de Andrade, V., Vidal, O., Jolivet, L., 2007. New, high-precision P-T estimates for Oman blueschists: implications for obduction, nappe stacking and exhumation processes. J. Metamorph. Geol. 25, 657–682. https://doi.org/10.1111/j.1525-1314.2007.00722.x.

Zamboni, D., Gazel, E., Ryan, J.G., Cannatelli, C., Lucchi, F., Atlas, Z.D., Trela, J., Mazza, S.E., De Vivo, B., 2016. Contrasting sediment melt and fluid signatures for magma components in the Aeolian Arc: implications for numerical modeling of subduction systems. Geochem. Geophys. Geosyst. 17, 2034–2053. https://doi.org/10.1002/2016GC006301.

Zarrinkoub, M.H., Pang, K.N., Chung, S.L., Khatib, M.M., Mohammadi, S.S., Chiu, H.Y., Lee, H.Y., 2012. Zircon U-Pb age and geochemical constraints on the origin of the Birjand ophiolite, Sistan suture zone, eastern Iran. Lithos 154, 392–405. https://doi.org/10.1016/j.lithos.2012.08.007.

Zong, K., Klemd, R., Yuan, Y., He, Z., Guo, J., Shi, X., Liu, Y., Hu, Z., Zhang, Z., 2017. The assembly of Rodinia: the correlation of early Neoproterozoic (ca. 900 Ma) high-grade metamorphism and continental arc formation in the southern Beishan Orogen, southern Central Asian Orogenic Belt (CAOB). Precambrian Res. 290, 32–48. https://doi.org/10.1016/j.precamres.2016.12.010.